

The Dryline on 22 May 2002 during IHOP: Ground-Radar and In Situ Data Analyses of the Dryline and Boundary Layer Evolution

MICHAEL S. BUBAN

Cooperative Institute for Mesoscale Meteorological Studies, University of Oklahoma, Norman, Oklahoma

CONRAD L. ZIEGLER

NOAA/National Severe Storms Laboratory, Norman, Oklahoma

ERIK N. RASMUSSEN

Cooperative Institute for Mesoscale Meteorological Studies, University of Oklahoma, Norman, Oklahoma

YVETTE P. RICHARDSON

Department of Meteorology, The Pennsylvania State University, University Park, Pennsylvania

(Manuscript received 26 January 2006, in final form 12 December 2006)

ABSTRACT

On the afternoon and evening of 22 May 2002, high-resolution observations of the boundary layer (BL) and a dryline were obtained in the eastern Oklahoma and Texas panhandles during the International H₂O Project. Using overdetermined multiple-Doppler radar syntheses in concert with a Lagrangian analysis of water vapor and temperature fields, the 3D kinematic and thermodynamic structure of the dryline and surrounding BL have been analyzed over a nearly 2-h period. The dryline is resolved as a strong ($2\text{--}4\text{ g kg}^{-1}\text{ km}^{-1}$) gradient of water vapor mixing ratio that resides in a nearly north-south-oriented zone of convergence. Maintained through frontogenesis, the dryline is also located within a gradient of virtual potential temperature, which induces a persistent, solenoidally forced secondary circulation. Initially quasi-stationary, the dryline retrogrades to the west during early evening and displays complicated substructures including small wavelike perturbations that travel from south to north at nearly the speed of the mean BL flow. A second, minor dryline has similar characteristics to the first, but has weaker gradients and circulations. The BL adjacent to the dryline exhibits complicated structures, consisting of combinations of open cells, horizontal convective rolls, and transverse rolls. Strong convergence and vertical motion at the dryline act to lift moisture, and high-based cumulus clouds are observed in the analysis domain. Although the top of the analysis domain is below the lifted condensation level height, vertical extrapolation of the moisture fields generally agrees with cloud locations. Mesoscale vortices that move along the dryline induce a transient eastward dryline motion due to the eastward advection of dry air following mesocyclone passage. Refractivity-based moisture and differential reflectivity analyses are used to help interpret the Lagrangian analyses.

1. Introduction

Surface boundaries such as fronts (e.g., Carbone 1982; Nielsen and Neille 1990), sea breezes (e.g., Laird et al. 1995; Kingsmill 1995), and thunderstorm outflows (e.g., Wakimoto 1982; Mahoney 1988) play an impor-

tant role in the initiation of deep convection, and thus have been extensively studied. The dryline has also become a subject of increasing interest due to its frequent association with convection initiation (CI) and subsequent development of severe weather in the southern Great Plains (Rhea 1966; Bluestein and Parker 1993). During the Verification of the Origins of Rotation in Tornadoes Experiment (Rasmussen et al. 1994), the structure of the dryline was observed in several cases (Atkins et al. 1998; Ziegler and Rasmussen 1998; Weiss and Bluestein 2002). Results from these and earlier ex-

Corresponding author address: Michael S. Buban, Forecast Research and Development Division, National Severe Storms Laboratory, 120 David L. Boren Blvd., Norman, OK 73072.
E-mail: michael.buban@noaa.gov

periments have improved the conceptual model of dryline morphology, though details of the temporal and spatial scales of the observations needed to predict CI are lacking. Despite a fairly good understanding of the mesoscale conditions that favor storm development, examination of the very small, kilometer-scale processes that force CI (Johns and Doswell 1992; McNulty 1995) has been hampered by a lack of high-resolution observations in previous studies.

During the spring and summer of 2002, the International H₂O project (IHOP) was conducted over the U.S. southern plains to gain a better understanding of the four-dimensional distribution of water vapor in the atmosphere (Weckwerth et al. 2004). One of the main objectives of this project was to obtain high resolution, small-scale observations of surface-based boundaries and the surrounding boundary layer (BL) to improve the understanding of cloud-scale CI processes and to contribute to development of improved short-range thunderstorm forecasts (Weckwerth and Parsons 2006).

Unlike boundaries such as fronts or thunderstorm outflows, which generally have strong temporal and spatial dynamical consistency, it has been postulated that the dryline dynamics and structure can vary markedly over very short time and space scales. For example, Bluestein et al. (1988) and Hane et al. (1997) show observational evidence and Ziegler et al. (1997) show from a three-dimensional numerical simulation that considerable horizontal along-line variability is present at the dryline. Other researchers have suggested that the dryline is modulated by vertical transport of westerly momentum (Ogura and Chen 1977; McCarthy and Koch 1982), symmetric instability (Ogura et al. 1982; Sun 1987), the inland sea-breeze effect (Ogura and Chen 1977; Ziegler et al. 1995; Atkins et al. 1998), and gravity waves (Koch 1979). The dynamics that govern dryline propagation are also unclear. It has been shown that at times the dryline may behave as a density current (Parsons et al. 1991; Ziegler et al. 1995; Atkins et al. 1998), while at other times the dryline may be forced by mixing and mesoscale advection processes (Schaefer 1974; Sun and Wu 1992). The temporal and spatial variability of the dryline and BL structure have significant implications for the convection initiation process.

During the late afternoon and early evening of 22 May 2002, high-resolution data were collected over the eastern Oklahoma panhandle in a region where a sharpening dryline had become established. Employing a multitude of observing platforms within a limited-area intensive observing region (IOR), a comprehensive cloud-scale observational dataset of the dryline and its BL environment was obtained. This paper employs

radar, in situ, and a newly developed Lagrangian analysis to describe the detailed structure and evolution of the dryline and surrounding BL and document the potential for convection initiation in the 22 May case. The Lagrangian analysis assimilates in situ state data via analyses of the time-varying 3D, multiple-Doppler wind field, facilitating the derivation of the evolving 3D thermodynamic structure of the dryline and the adjacent BL. Refractivity and polarimetric radar measurements are used, respectively, to estimate surface moisture fields and to infer the extent of the moist BL and secondary circulations along the dryline.

2. Data collection and analysis

a. IHOP facilities

The IHOP mobile facilities were deployed on the afternoon of 22 May 2002 in the eastern Oklahoma panhandle in the anticipation of CI in the vicinity of a developing dryline (Fig. 1a). The dryline began as a weak moisture gradient, which progressively strengthened throughout the afternoon. Although there was the potential for deep convection, storms failed to form from the developing cumuli in the IOR.

Among the platforms participating in the data collection were seven mobile mesonets, which obtained in situ measurements of temperature, relative humidity, pressure, and wind velocity (Straka et al. 1996; Ziegler et al. 2004; Buban 2005). Each mobile mesonet (MM) performed east–west transects approximately perpendicular to the dryline (Fig. 1b) and collected data at a frequency of 1 Hz. The 5-cm Shared Mobile Atmospheric Research and Teaching (SMART) radar or SR1 (Biggerstaff et al. 2005) was deployed with the 3-cm Doppler on Wheels (DOW) DOW2, DOW3, and X-band dual polarization Doppler (X-Pol) radars (Wurman et al. 1997; Wurman 2001). The mobile ground-based radars were arrayed in a diamond pattern (Fig. 1b), with each radar taking time-synchronized 140° sector scans stepped in elevation and centered on the dryline and completing volumes in 1.5–3 min (Table 1). This configuration was employed to maximize baseline angles and allow for optimal multiple-Doppler wind synthesis. Between 2230 and 0100 UTC, three to four mobile radars were obtaining data in the IOR (Table 2). The present study also uses data from a mobile Cross-Chain Loran Atmospheric Sounding System (CLASS; Rust et al. 1990) and two mobile GPS/Loran Atmospheric Sounding System (GLASS) vehicles, the Wyoming King Air, the Naval Research Laboratory P-3, and a combination of fixed soundings and scanning Raman lidar (SRL) profiles at the Homestead site (Demoz et al. 2006). A ground-based digital camera provided cloud field images from a sedan (CAM1).

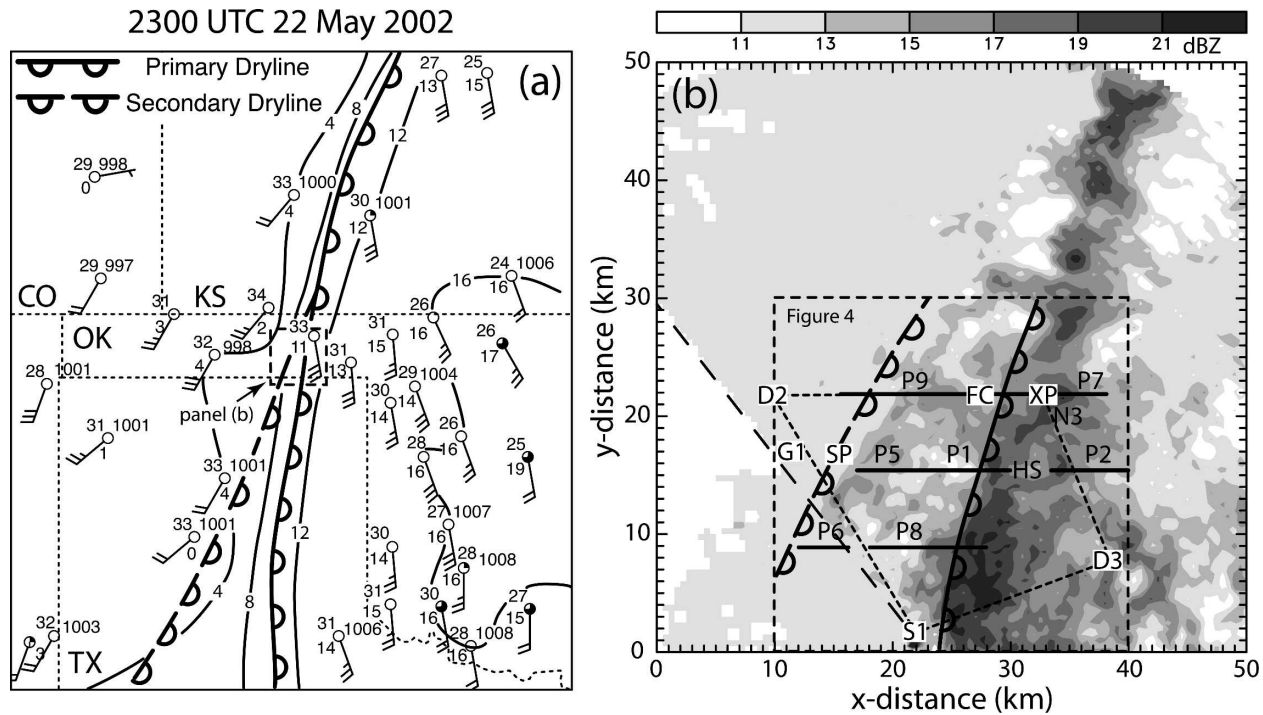


FIG. 1. Surface conditions at 2300 UTC 22 May 2002. (a) Surface map with standard station models and subjectively analyzed dewpoint (solid black lines, °C). (b) Radar reflectivity (dBZ) in the radar analysis domain including the locations of the radars and mobile mesonet legs. The location of the radar analysis domain is shown by the dashed box in (a). The black dashed box in (b) is the thermodynamic analysis domain. The long dashed line indicates the edge of SR1 data. In both panels, the locations of the primary dryline (solid line with semicircles) and the minor dryline (dashed line with semicircles) are shown. Platform abbreviations are as follows: Field Coordination vehicle (FC), Probe 1, 2, . . . (P1, P2, . . .), DOW2 (D2), DOW3 (D3), X-Pol (XP), S-Pol (SP), SMART radar (S1), mobile CLASS (N3), mobile GLASS (G1), and Homestead location (HS).

Given the proximity of the IOR to the Homestead, Texas, and S-band dual polarization Doppler radar (S-Pol) sites, both Homestead soundings and S-Pol radar data were used to complement the mobile observations (Fig. 1b). Additional observations were obtained from a Learjet releasing dropsondes, the University of Alabama in Huntsville Mobile Integrated Profiling System (MIPS; Karan and Knupp 2006), and a mobile microwave radiometer. Weiss et al. (2006) analyzed transects of the 22 May dryline using a mobile vertically scanning Doppler radar.

b. Radar analysis

In the first step of the radar postanalysis, described in detail by Ziegler et al. (2007), the data are edited using

TABLE 1. Radar specifications for the four mobile Doppler radars participating in the data collection on 22 May 2002.

Radar specifications	SR1	DOW2	DOW3	X-Pol
Beamwidth (°)	1.5	0.95	0.95	0.95
Gate spacing (m)	67	75	75	210
Volume scan rate (min)	2.0	1.3	1.3	1.3
Scan volume spacing (min)	3	1.5	1.5	1.5

SOLO (Oye et al. 1995) to correct truck orientation relative to north by either of two methods. For DOW2, an offline algorithm is applied to determine truck orientation by comparing the angle of the maximum power returned on a sweep scanning the sun with the known orientation of the sun relative to true north (Arnett et al. 2003). For the other radars, a geographic information system-based technique is applied to rotate

TABLE 2. Participating mobile Doppler radars (marked with an “x”) during various analysis time periods from 2233 to 0024 UTC 22 May 2002. Data were collected by at least one radar between 2230 and 0100 UTC.

Analysis interval	SR1	DOW2	DOW3	X-Pol	Tot radars
2233–2251 UTC		x	x	x	3
2254–2257 UTC	x	x	x	x	4
2300–2312 UTC	x	x	x		3
2315 UTC	x	x	x	x	4
2318–2342 UTC	x	x	x		3
2345–2351 UTC	x	x	x	x	4
2354–0012 UTC	x	x	x		3
0015 UTC	x	x	x	x	4
0018–0024 UTC	x	x	x		3

TABLE 3. Barnes filter parameters and response values at selected wavelengths (km) or periods (min) for the temporal and spatial Barnes weighting in the radar and Lagrangian objective analyses. The filter parameter (Barnes 1973; Koch et al. 1983) is denoted by κ for spatial weighting and τ for temporal weighting. The radar analysis applies one filtering pass of the Barnes interpolation, while the convergence parameter $\gamma = 0.3$ for the two-pass Lagrangian objective analysis. The corresponding response functions are displayed in Fig. 2.

Type of data being interpolation	Barnes filtering parameter	Wavelength (km)/period (min) for 5% response	Wavelength (km)/period (min) for 80% response
Spatial radar observation	$\kappa = 0.0486$	0.4 km (one pass)	1.4 km (one pass)
Spatial Lagrangian point	$\kappa_s = 0.076$	0.25 km (second pass)	0.75 km (second pass)
Temporal initial condition	$\tau_i = 364\ 363$	10 min (second pass)	29 min (second pass)
Temporal Lagrangian point	$\tau_L = 640\ 856$	13 min (second pass)	39 min (second pass)

radar sweeps to match ground targets in the radar data with known locations of the targets (Ziegler et al. 2004). The data are also edited with SOLO to remove ground targets and weak signals and to dealias radial velocities.

The REORDER single radar analysis software (Oye et al. 1995) is used to interpolate the edited data to a $50 \times 50 \times 2.5$ km regular Cartesian grid with a grid spacing of 500 m in the horizontal and 250 m in the vertical ($101 \times 101 \times 11$ grid points). The interpolation is performed using a Barnes objective analysis scheme with a weighting function $w_r = \exp(-r^2/\kappa)$, where r is the distance between a weighted datum and the grid-point and κ is the smoothing parameter which controls the shape of the response function (Koch et al. 1983). Choosing $\kappa = 0.0486$ yields a 5% analysis response at a wavelength $\lambda = 0.4$ km and an 80% response at $\lambda = 1.4$ km (Table 3, Fig. 2). The Barnes weighting function has been chosen to capture the cloud-scale (~ 1 km) features of the flow while damping the influence of smaller unresolvable scales.

The objectively analyzed velocity data are then combined using the Custom Editing and Display of Reduced Information in Cartesian Space (CEDRIC) software (Mohr et al. 1986) to iteratively solve an overdetermined set of two linear equations and mass continuity to obtain the triple- or quadruple-Doppler wind velocity field $\mathbf{v}(x, y, z) = u\mathbf{i} + v\mathbf{j} + w\mathbf{k}$. The vertical velocities are obtained by integrating the anelastic mass continuity equation upward assuming $w = 0$ at ground level. Time series of triple- or quadruple-Doppler-synthesized three-dimensional wind velocities are produced at 3-min intervals from 2233 to 0024 UTC (Table 2).

c. Lagrangian analysis of thermal variables

In situ data collected from the mobile mesonets, aircraft, and soundings are used to infer the thermodynamic characteristics of the dryline and surrounding BL. Because in situ data are collected along one-dimensional transects (i.e., east–west roads, a flight leg)

the horizontal resolution is limited by platform spacing. To circumvent this problem, a time-to-space conversion procedure has been developed to extract instantaneous 3D spatial fields from strings of 1D data in space and time. According to this Lagrangian objective analysis technique (Ziegler et al. 2007), these in situ data are assigned at “Lagrangian points” along individual upstream and downstream trajectories that are initiated from a given datum location and computed from the time-varying multiple-Doppler synthesized wind fields assuming local conservation following the motion.

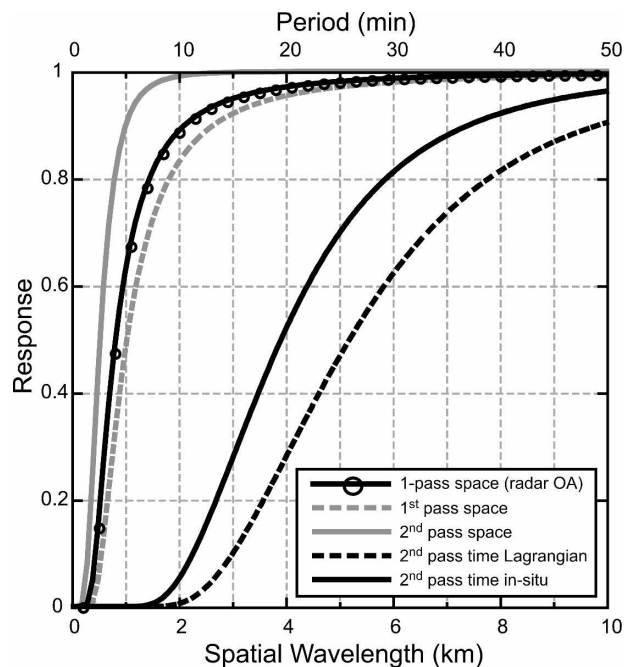


FIG. 2. Theoretical Barnes spectral response functions of the Lagrangian analysis. The responses as functions of wavelength (km) are shown for the one-pass radar objective analysis (solid line with circles) and the first pass (dashed gray) and second pass (solid gray) spatial weighting. Also shown are the theoretical Barnes responses of the second pass Lagrangian (dashed black) and second pass in situ (solid black) temporal Lagrangian weighting as a function of period (min).

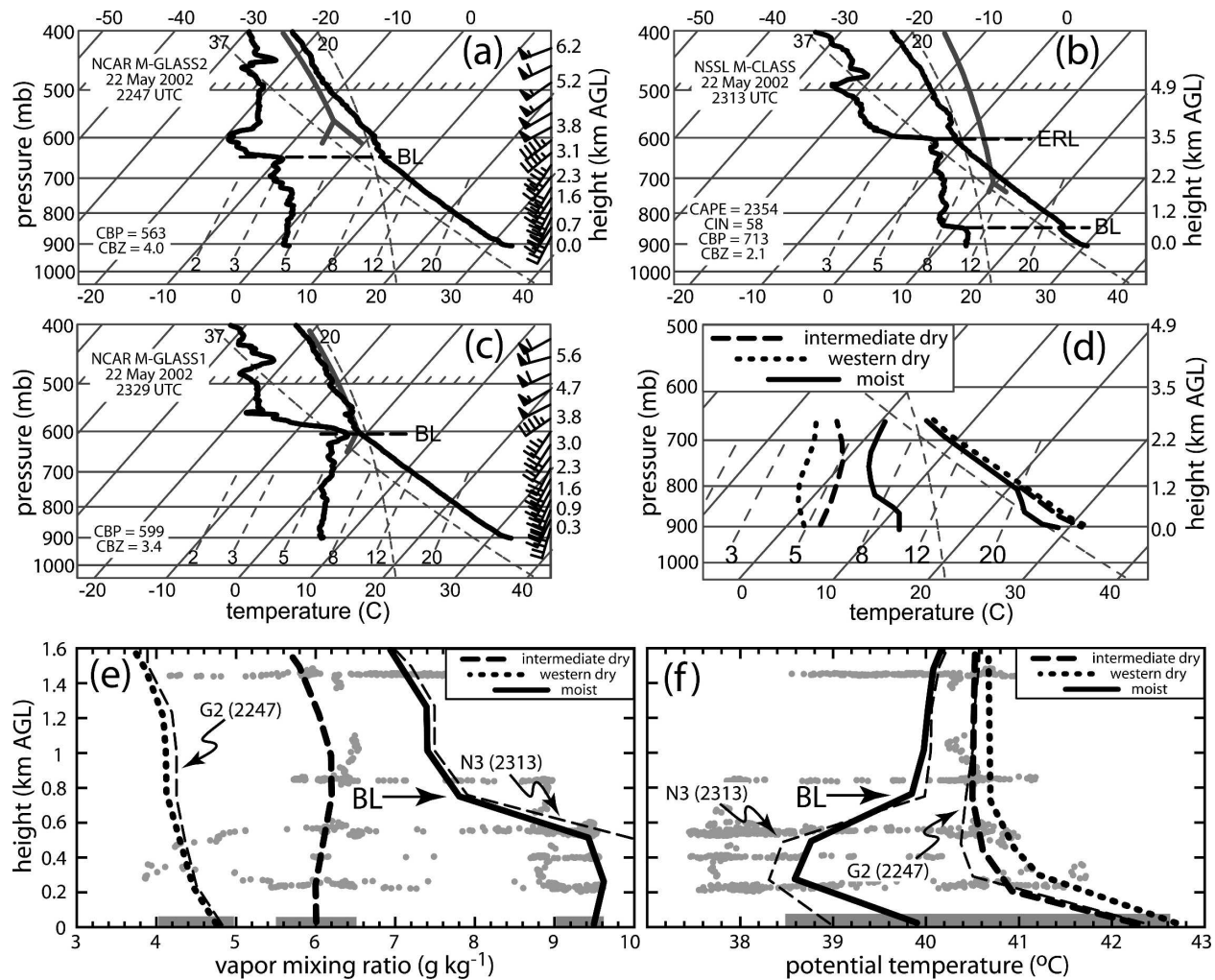


FIG. 3. Mobile soundings launched on 22 May 2002. (a) 2247 UTC National Center for Atmospheric Research (NCAR) GLASS sounding launched west of the western minor dryline; (b) 2313 UTC National Severe Storms Laboratory (NSSL) CLASS sounding launched east of the primary dryline; (c) 2329 UTC NCAR GLASS sounding launched between the western minor and primary drylines; (d) the reference soundings derived from observed soundings and used in the Lagrangian analyses; (e) vapor mixing ratio profiles vs King Air observations; (f) same as (e) but for potential temperature. Indicated sounding parameters, derived from parcel theory using the lowest 50-mb-average parcel, include CAPE, CIN, cloud-base pressure (CBP), and cloud-base height (CBZ). The labels BL and ERL indicated the top of each layer.

The Lagrangian analysis proceeds in multiple steps as follows. In the initial step, the advected MM data are analyzed on the surface grid using a 2D Barnes objective analysis. The generalized Barnes weighting function for Lagrangian analysis takes the form $w = \exp[-(r^2/\kappa_s) - (t_i^2/\tau_i) - (t_L^2/\tau_L)]$, where t_i and t_L are, respectively, the time difference between an observation and the nominal analysis time and the accumulated Lagrangian integration time. The parameters κ_s , τ_i , and τ_L are the spatial and two temporal smoothing parameters, respectively (Table 3). In the second analysis step, air mass reference soundings (Figs. 3d–f) are used to derive local pseudosoundings (or grid-

column soundings) that are produced by mixing percentages of the moist- and dry-side reference soundings depending on the local 2D surface analysis mixing ratio value. Although Ziegler et al. (2007) assumed a single reference sounding west of the dryline, the present study includes a second dry-side reference sounding to better represent the BL heterogeneity. For example, if the moist (dry) side surface sounding value is 8 (4) g kg^{-1} and the grid point surface analysis value is 7 g kg^{-1} , the resulting pseudosounding would consist of a mixture of 75% of the moist side sounding and 25% of the dry side sounding. Generalizing the method described by Ziegler et al. (2007), the local (i.e., in the x

direction) midpoint between the primary (eastern) and weaker (western) drylines in the 2D surface analysis is used to discriminate which reference sounding pair to apply in a given grid column. Grid-column soundings are applied only in mesoscale updrafts, thus representing the local surface conditions. Trajectories are calculated from individual grid points in these grid-column soundings, followed by 3D Barnes objective analyses of all in situ and grid-column sounding data. In this manner, conditions in mesoscale downdrafts are prescribed via grid-column sounding data extrapolated from adjacent updrafts. A second 3D Barnes objective analysis pass is applied with a convergence parameter $\gamma = 0.3$ to recover additional detail from the combined Lagrangian data (Fig. 2).

In a special application of the Lagrangian analysis to be presented in section 4d, the misocyclone-relative airflow is used to compute surface, grid-column, and lateral inflow boundary trajectories in a subdomain that follows a misocyclone of interest. The principle purpose of using misocyclone-relative airflow is to decrease the truncation error of the linear time interpolation between successive wind analyses by minimizing the contribution to the local time derivative due to vortex motion. In this special Lagrangian analysis application in the vortex-containing subdomain, the grid-column trajectories are initialized from the full-domain, two-pass Lagrangian analysis values described previously. A second two-pass analysis is then conducted in the nested domain by employing the same spatial and in situ smoothing parameter values used in the full-domain analysis along with a Lagrangian smoothing parameter about 10% of the value listed in Table 3. Thus, the nested Lagrangian analysis effectively increases the resolution of along-Lagrangian variability in a time-to-space sense.

Some limitations of the Lagrangian analysis technique should be discussed before interpreting the results. The analyses assume that data from a finite-width time window globally represent conditions at the nominal analysis time via the data's time-to-space position adjustment effected by the forward or backward trajectories. The analyses are influenced most heavily by the mobile mesonet observations, as these are the most spatially and temporally dense. The density of observations controls the amount of detail in the analyses. Although data spacing was small between observations for a given mobile mesonet, spacing between mesonets was large (~ 6 km). Because the flow was nearly perpendicular to the mesonet legs, small-scale along-wind temperature and moisture gradients were poorly sampled, and thus must be filtered to emphasize only

the resolvable along-flow scales. To partially ameliorate the filtering effect of along-Lagrangian weighting as explored in section 4d, the smoothing of the wrapping patterns of moist and dry air generated by horizontal advection around a small dryline misocyclone may be reduced by effectively increasing the number of filtering passes. The kinematic aspects of these gradients were effectively resolved due to the 500 m along-wind multiple-Doppler analysis grid spacing. The temporal and spatial Barnes objective analysis parameters (Table 3) were chosen to yield optimal results for the given data spacing. The extent to which the reference soundings are locally representative determines the accuracy of the analyses. Gridpoint sounding data and in situ aircraft data (Ziegler et al. 2007) show good comparisons (e.g., Figs. 3e,f) and thus justify the use of the reference soundings.

3. Analysis results

a. Synoptic setting

The large-scale pattern on the afternoon of 22 May exhibited a broad low-amplitude ridge over the central United States situated between a departing shortwave trough over the southeast and an approaching trough over the northern intermountain west (Weiss et al. 2006). This pattern featured broad west-southwesterly flow at upper levels and south-southwesterly to southerly flow at low levels over the central and southern plains. A surface trough and moisture gradient had developed in the lee of the Rockies from Nebraska southward through Texas, and by afternoon had strengthened to form a pronounced dryline (Fig. 1a). The low levels were warm and moist to the east of the dryline (Figs. 1a, 3b)—while possessing appreciable convective available potential energy (CAPE)—and hot and dry to the west of the dryline (Figs. 1a, 3a, 3c). It will subsequently be shown that bands of high-based cumulus clouds developed in the vicinity of the dryline by mid-afternoon. From late afternoon through early evening, the cumulus clouds continued to form but were unable to overcome the convective inhibition (CIN) to realize the high CAPE and form storms. The dryline started moving west during the late afternoon. Two key aspects of the inhibition of convection were the large difference between the level of free convection and the BL top coupled with the warm, dry, highly sheared conditions in that layer, as in the 7 June 1994 case examined by Ziegler and Rasmussen (1998).

b. Radar observations

The dryline is delineated by a nearly north-south-oriented band of enhanced reflectivity residing in a

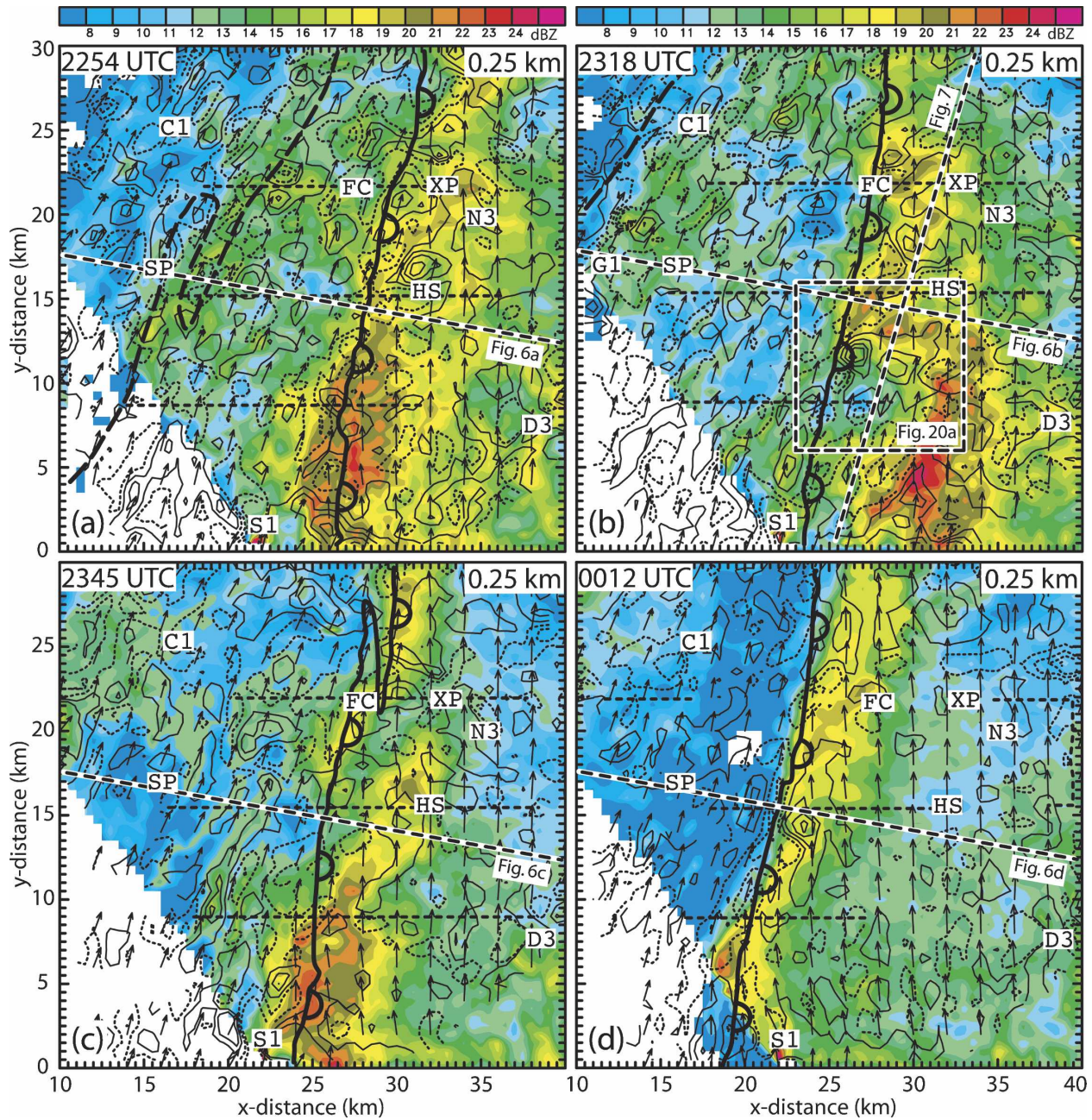


FIG. 4. Radar analysis fields at 0.25 km AGL at (a) 2254, (b) 2318, (c) 2345, (d) 0012 UTC 22 May 2002. Reflectivity (dBZ), horizontal wind vectors (every fourth grid point with 1-km vector length equal to 15 m s^{-1}), and vertical vorticity (s^{-1}) every $2 \times 10^{-3} \text{ s}^{-1}$ with positive values (black solid lines) starting at $1 \times 10^{-3} \text{ s}^{-1}$ and negative values (black dotted line) starting at $-1 \times 10^{-3} \text{ s}^{-1}$. Also labeled are the locations of the Field Coordinator vehicle (FC), the digital camera (C1), the mobile GLASS (G1), and CLASS (N3) sounding systems, DOW3 (D3), X-Pol (XP), the SMART radar (SR1), and Homestead (HS). The thin dashed lines locate the mobile mesonet legs. The thick dashed black lines indicate the locations of cross sections shown in Figs. 6, 7, and 21. The positions of the primary (thick scalloped curve) and minor (thick dashed curve) drylines as determined by the thermodynamic analyses are also shown as in Fig. 1, including the 2251 UTC dryline positions in (a).

zone of confluent flow (Fig. 4). The low-level winds are southerly to the east of the dryline, while the winds are southwesterly to the west of the dryline. The winds veer to southwesterly at the top of the BL, orienting the

dryline nearly along the mean BL flow. Although the orientation of the dryline is toward about 10° east of north, several undulations in the reflectivity and velocity gradients indicate that smaller dryline segments may

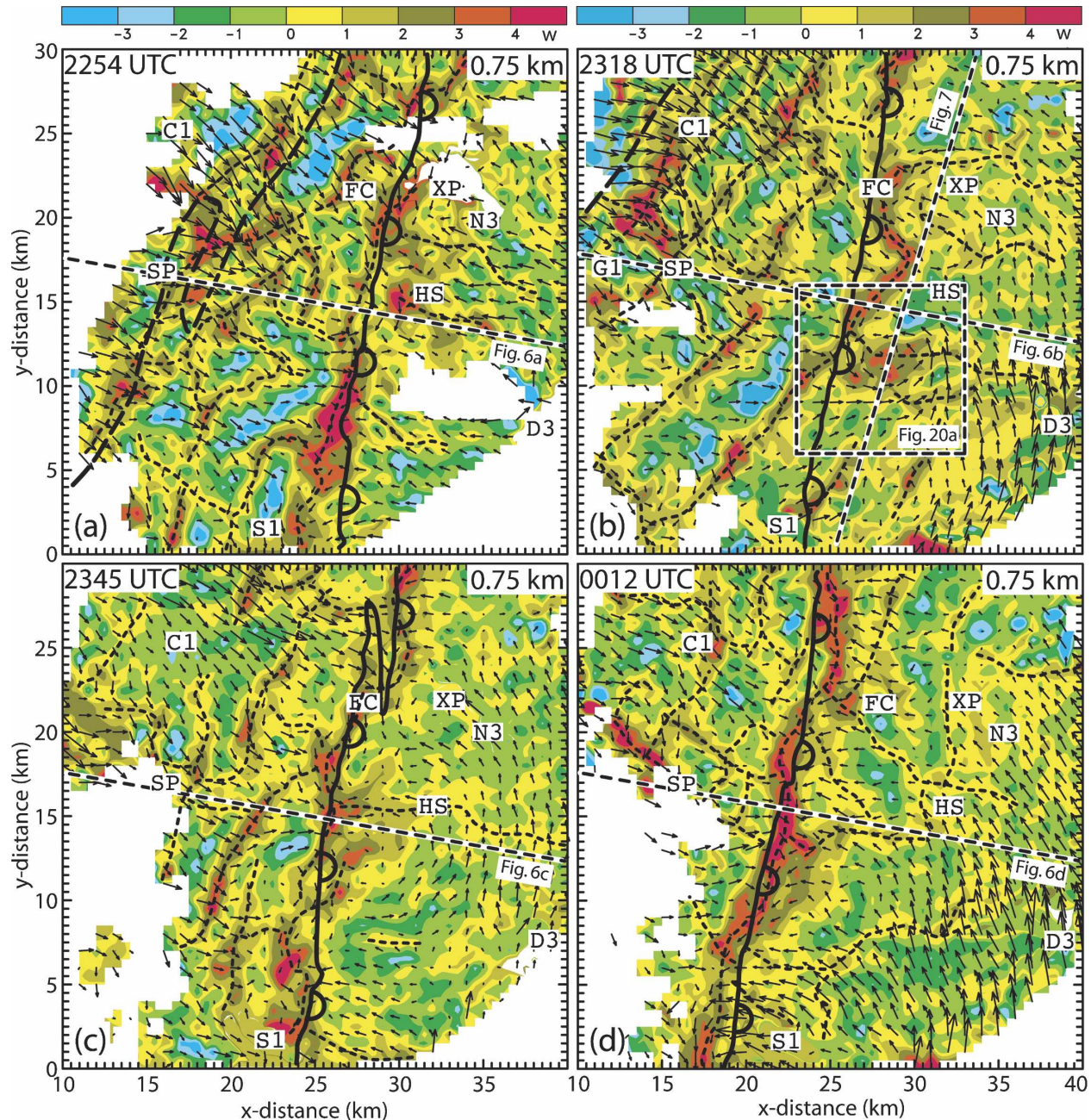


FIG. 5. Vertical velocity (shaded) and horizontal wind vectors (every other grid point with 1-km vector length equal to 5 m s^{-1}) at 750 m AGL: (a) 2254, (b) 2318, (c) 2345, and (d) 0012 UTC. The vortex-relative flow field was obtained by subtracting the mean misovortex motion from 194° at 20.6 m s^{-1} from the horizontal ground-relative winds. The black dashed lines indicate locations of convective bands and the black dashed box in (b) shows the location of Fig. 20a. The dryline locations determined from the thermodynamic analyses are as in Fig. 4.

exhibit different orientations. These undulations are on the order of 10 to 15 km in wavelength, and appear to ripple along the dryline with the low-level flow. A second, minor dryline is located about 10 to 15 km west of the primary dryline (see also Fig. 1 for the synoptic setting of the details), and exhibits a secondary local

reflectivity maximum in a zone of confluence. It will be shown later that the minor dryline is associated with a weaker moisture gradient than the primary dryline.

The BL airflow structure changes markedly during the period between 2254 and 0012 UTC (Fig. 5). The south-southwest to north-northeast-oriented dryline is

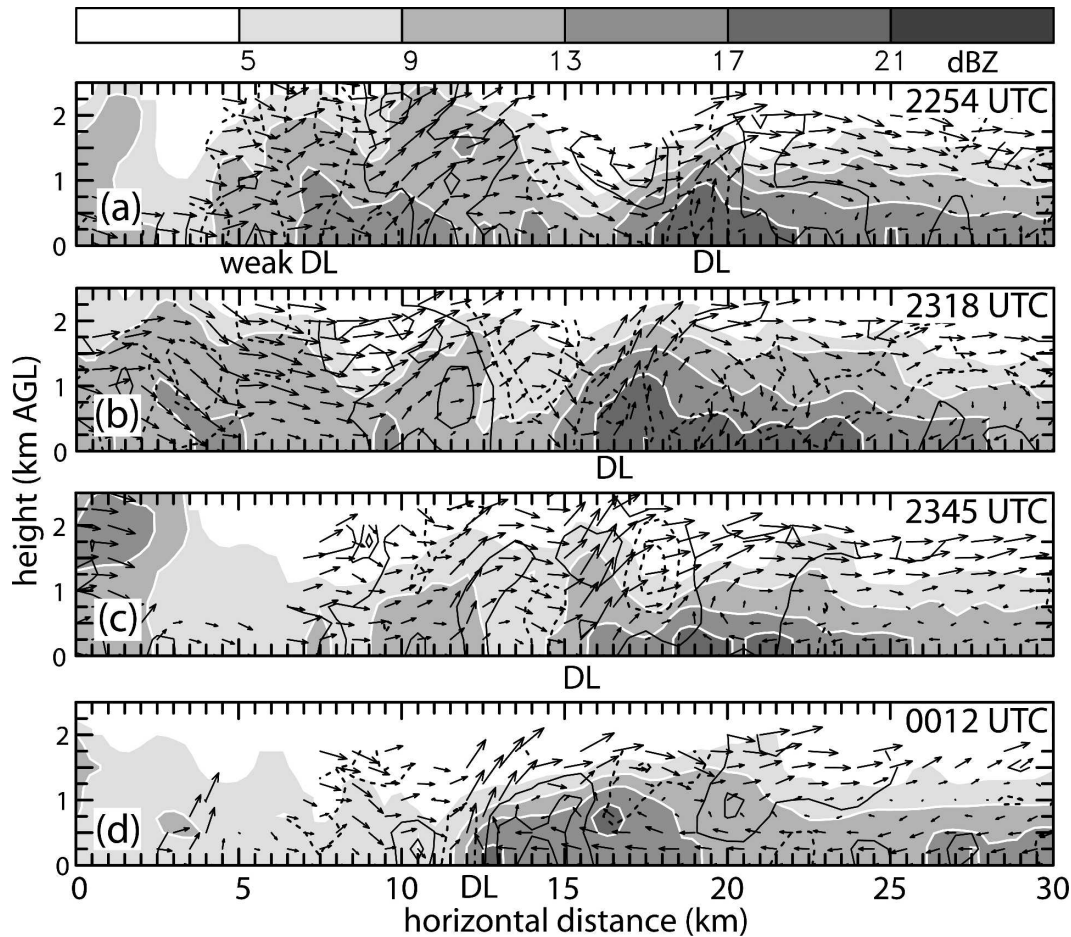


FIG. 6. Vertical dryline-normal cross sections of reflectivity (dBZ), ground-relative wind vectors with 1-km length equal to 10 m s^{-1} , and vertical vorticity (s^{-1} , every $2 \times 10^{-3} \text{ s}^{-1}$) with positive values (black solid lines) starting at $2 \times 10^{-3} \text{ s}^{-1}$ and negative values (black dotted line) starting at $-2 \times 10^{-3} \text{ s}^{-1}$. Cross section locations are indicated in Fig. 4.

initially quasi-stationary, located near X-Pol and Homestead, and seen as a nearly continuous zone of moderate updrafts with embedded pockets of updrafts greater than 2 m s^{-1} . The BL west of the dryline exhibits a complex structure characterized by both open cellular and longitudinal horizontal convective roll (HCR) circulations. A complex pattern of east-west-oriented bands of enhanced vertical velocity associated with transverse rolls develops to the east of the dryline. A band of stronger updrafts is also associated with the minor dryline.

As the dominant convective mode becomes more organized into HCRs west of the dryline, several undulations of reflectivity (Fig. 4) and updraft (Fig. 5) develop in the regions of dryline-HCR or dryline-transverse roll intersections and propagate northward along the dryline. These undulations have wavelengths on the order of 7–8 km and in several instances are collocated

with mesocyclones. With the loss of surface heating around 0000 UTC, the HCRs in the dry air become less organized as the winds in the moist air back, the dryline updraft strengthens, and the dryline accelerates westward. The smaller-scale waves that rippled along the dryline are replaced with larger ($\sim 15\text{-km}$ wavelength) waves after retrogression begins. As with the smaller-scale waves, the longer waves also propagate along the dryline at a speed close to the mean BL wind. These waves, termed mesoscale dryline waves (MDLWs; Koch and McCarthy 1982), are similar in wavelength to MDLWs reported by McCarthy and Koch (1982).

A strong dryline-normal secondary circulation is evident through the entire analysis period (Fig. 6). The term secondary circulation is used to denote an ageostrophic perturbation circulation in the plane normal to the dryline (Ziegler et al. 1995). The strong south-southwesterly flow approaches the dryline from the

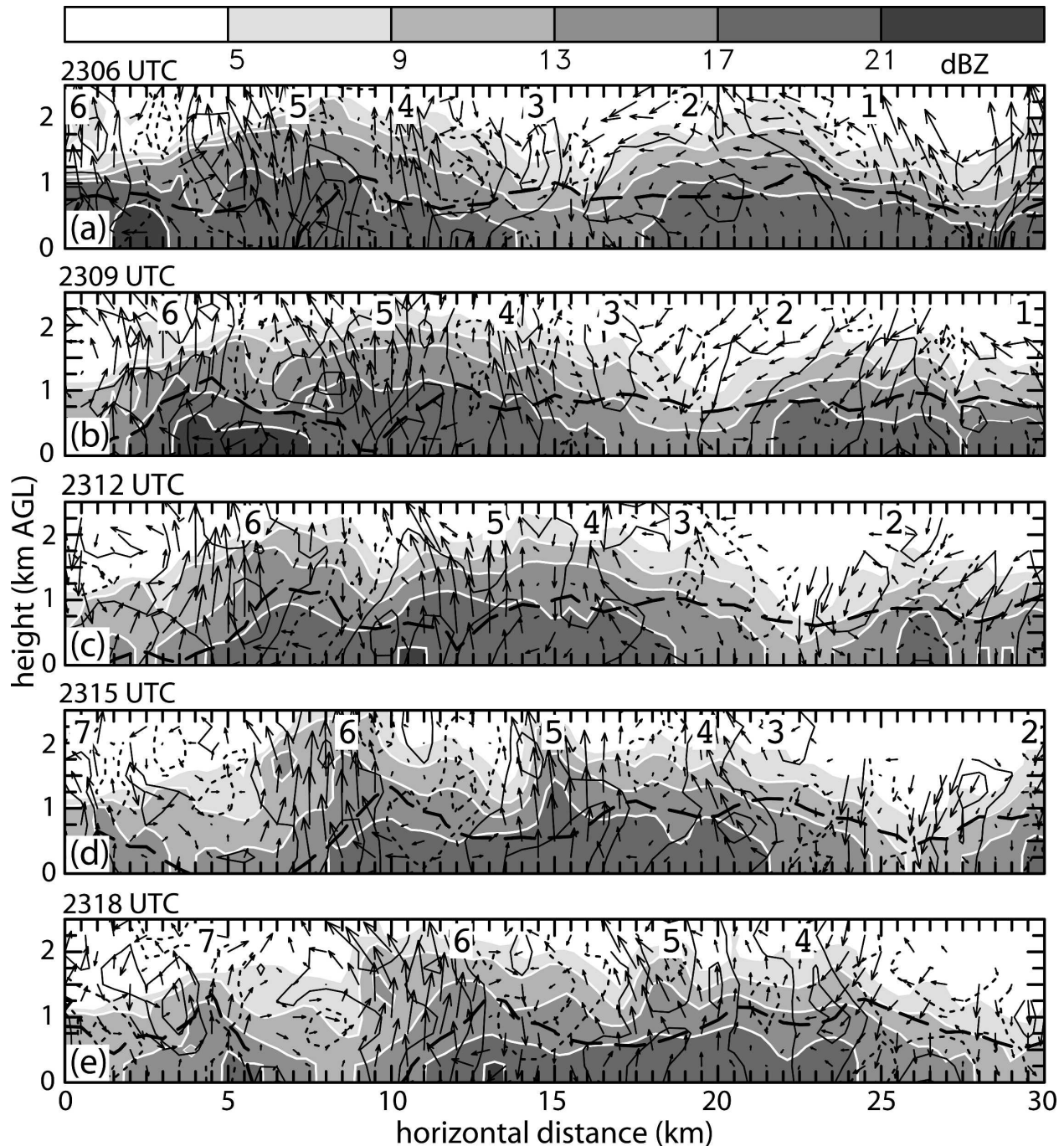


FIG. 7. Vertical dryline-parallel cross sections of reflectivity (dBZ), misocyclone-relative wind vectors (1-km length equal to 5 m s^{-1}), and vertical vorticity (s^{-1}) every $2 \times 10^{-3} \text{ s}^{-1}$ with positive values (black solid lines) starting at $2 \times 10^{-3} \text{ s}^{-1}$ and negative values (black dotted line) starting at $-2 \times 10^{-3} \text{ s}^{-1}$. Above (below) the long dashed black line, the flow is greater than (less than) zero out of (into) the plane. A constant reference horizontal wind, from 194° at 20.6 m s^{-1} , was subtracted from the wind vectors to better identify circulations. Cross section locations are indicated in Fig. 4. Individual transverse rolls are numbered in order of appearance.

west, converging with the southerly low-level jet, and strong updrafts lift the westerly flow over the surface dryline location. An opposing flow at low levels east of the dryline associates with westerly BL flow separation

from the surface, while elevated westerly flow subsequently exits the updraft. Ziegler and Rasmussen (1998) hypothesized that air parcels rising in the dryline updraft must achieve their lifted condensation level

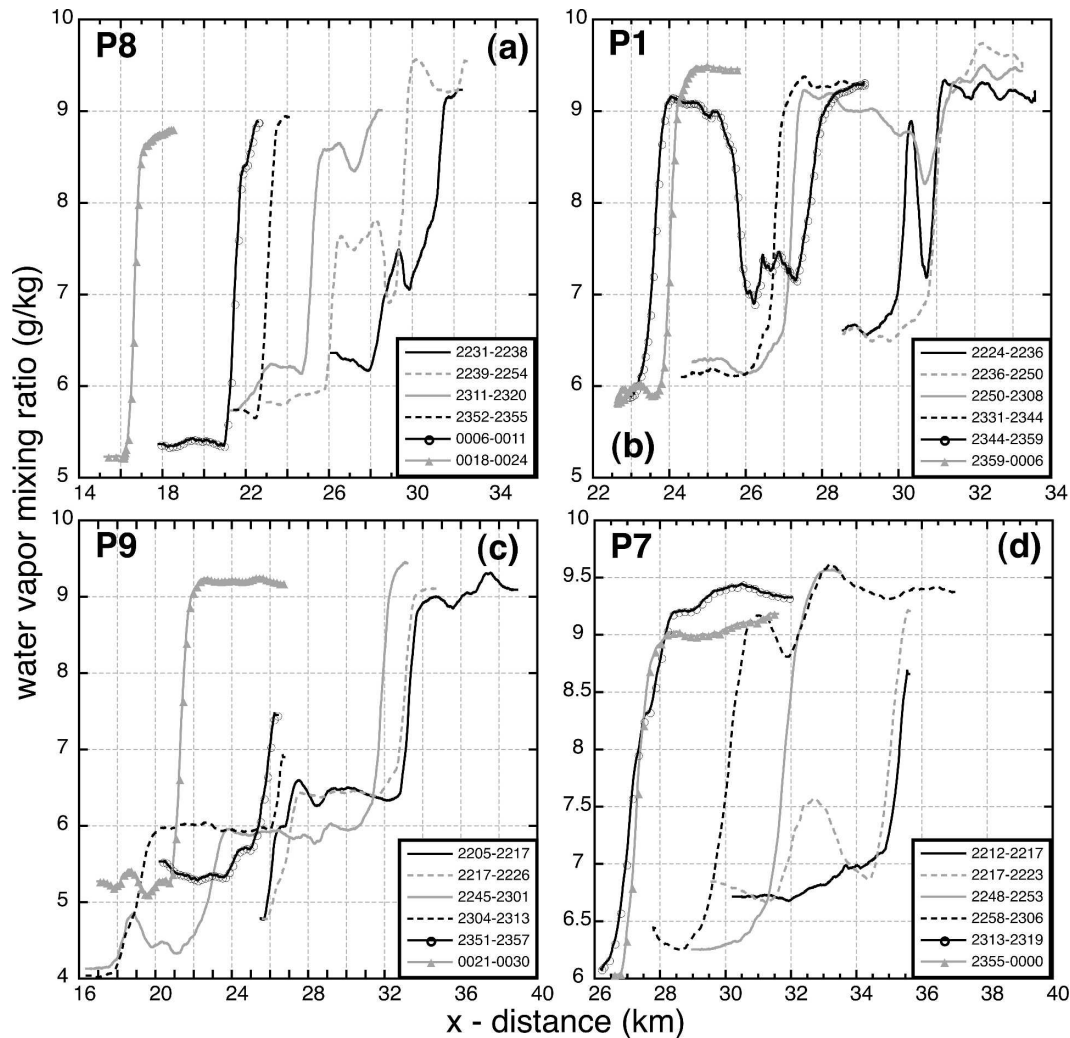


FIG. 8. Mobile mesonet traverses of water vapor mixing ratio (g kg^{-1}) as a function of horizontal distance (km) in the radar analysis grid during the times indicated in the lower-right-hand corner from: (a) probe 8, (b) probe 1, (c) probe 9, and (d) probe 7. Probe 8 was located on the southern road, probe 1 on the center road, and probes 9 and 7 on the northern road as depicted in Figs. 1 and 4.

(LCL) before exiting the updraft to form a cumulus cloud. The vertical velocity maximum at the dryline is consistent with a maximum in reflectivity as insect scatterers are concentrated and lofted in the updraft (Geerts and Miao 2005b). The highest reflectivities are generally contained within the boundary layer east of the dryline.

The BL east of the dryline contains transverse rolls that move northward (Figs. 5 and 7). The transverse rolls move rather uniformly from 194° at a speed of around 21 m s^{-1} , or approximately the velocity of the mean low-level flow. Enhanced vertical vorticity is collocated with the roll updrafts, leading to the speculation of vorticity growth proceeding from stretching amplification of some combination of preexisting vertical vor-

ticity or vertical vorticity produced by tilting of the along-roll component of the ambient BL shear.

Numerous 1–3 km scale misocyclonic vortices are contained in the BL, and high concentrations of misovortices are observed near the dryline (Fig. 4). The vorticity values in the stronger misocyclones are in the range of $3\text{--}9 \times 10^{-3} \text{ s}^{-1}$, effectively approaching the order of magnitude of low-level thunderstorm boundary layer mesocyclones (Wakimoto et al. 1998; Ziegler et al. 2001). Similar to the transverse rolls and the dryline waves, these misovortices also tend to move with the mean low-level BL flow. Both the dryline waves and misocyclones display temporal and spatial continuity in animation of the 3-min interval analyses. Because the individual radar analyses are independent,

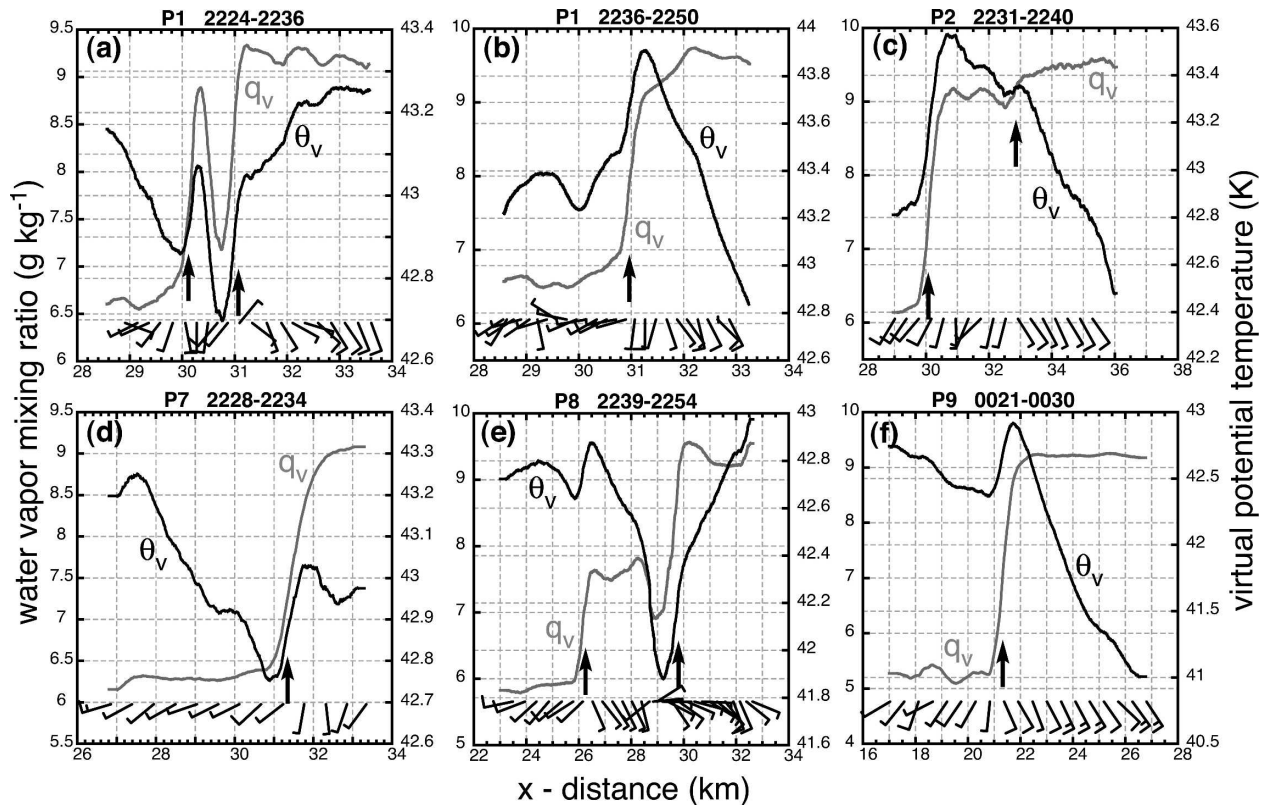


FIG. 9. Water vapor mixing ratio (gray curve), virtual potential temperature (black curve), and winds during individual mobile mesonet dryline traverses. (a) Probe 1 from 2224 to 2236 UTC, (b) probe 1 from 2236 to 2250 UTC, (c) probe 2 from 2231 to 2240 UTC, (d) probe 7 from 2228 to 2234 UTC, (e) probe 8 from 2239 to 2254 UTC, and (f) probe 9 from 0021 to 0030 UTC. Misovortex-relative winds (ground-relative mesonet wind minus 194° at 20.6 m s^{-1} wind vector) are shown below the curves with a full barb equal to 5 m s^{-1} and a half barb equal to 2.5 m s^{-1} . Arrows locate moisture gradients referred to in the text.

the observed continuity of features implies fidelity of the individual analyses and a degree of airflow predictability.

c. Mobile mesonet observations

The mobile mesonets typically measure across-dryline mixing ratio gradients of about $3\text{--}4 \text{ g kg}^{-1} \text{ km}^{-1}$ (Fig. 8), similar to values reported by Ziegler and Rasmussen (1998) and Pietrycha and Rasmussen (2004). The west–east dryline profiles (i.e., from dry to moist) measured by the mobile mesonets are classifiable into three distinct types. The first type is characterized by a single steplike moisture increase over about 1 km (e.g., P8, 0018–0024 UTC traverse in Fig. 8a; P7, 2355–0000 UTC traverse in Fig. 8d). The second type, characterized by two distinct steps in the moisture field (e.g., P9, 2205–2217 UTC in Fig. 8c), has previously been referred to as a double dryline (Hane et al. 1993; Hane et al. 2001). These dryline profiles are analogous to the type 2 profiles measured by the P-3 and King Air (e.g., Demoz et al. 2006). The third type is characterized by a sudden moisture rise followed by a sudden drop, then

another sudden rise on the moist side of the dryline (e.g., P1, 2344–2359 UTC in Fig. 8b). The amplitude of the intermediate moisture drop in the type 3 profile varies from transect to transect. It is speculated that the steplike dryline profiles can be explained by horizontal and vertical transport and the local state of mixing within the evolving secondary circulation (Ziegler and Hane 1993). For example, downward transport of dry air may locally weaken or eliminate the moist layer just ahead of the dryline, producing a steplike moisture profile across the two boundaries (e.g., 15 May 1991 dryline, Ziegler and Rasmussen 1998; 16 May 1991 thin-line–dryline, Hane et al. 2001). Complicated across-dryline profiles were also documented by Crawford and Bluestein (1997) and Pietrycha and Rasmussen (2004).

The virtual potential temperature (θ_v) profile is typified by higher values on the dry side than on the moist side of the classic type 1 dryline, with a local maximum residing in the moisture gradient (Figs. 9b,c,d,f). Typical cross-dryline θ_v gradients are about 0.25 K km^{-1} , with absolute differences (i.e., warmest to coolest) between 0.5 and 2 K. The local θ_v maximum along the

dryline varies from relative (Fig. 9d) to absolute (Figs. 9b,c,f) as a consequence of the relative changes in θ and q_v , and may be important for virtual buoyancy in the surface layer. Type 2 and type 3 profiles (Figs. 9e and 9a, respectively) have similar temperature maxima on the moist side of the moisture gradients, although both types have temperature minima associated with adjacent q_v minima. The local θ_v maxima reflect the moisture effect on virtual temperature for small potential temperature changes at the leading edge of the dryline. Collocation of θ_v and q_v minima (Fig. 9a,e) may indicate flushing by downdrafts (Ziegler et al. 1997) in an unstably stratified lower BL in which q_v also decreases with height (Fig. 3). The collocation of θ_v maxima and updrafts around the dryline may be dynamically significant, as these warm plumes would be potentially buoyant relative to the adjacent BL. The persistence and location of the θ_v gradient relative to the q_v gradient may determine if the solenoidally forced updraft will primarily lift dry or moist surface layer air.

Mobile mesonet wind measurements typically indicate south to southeasterly misovortex-relative winds to the east of the dryline and west to southwest winds to the west of the dryline (Figs. 9b,c,d,f), with the main confluence zone located in the largest moisture gradient. Two of the dryline transects indicate sharp local drying and cooling concurrent with a rapid backing of the winds to northeasterly (Figs. 9a,e), while another confluence band is associated with the westernmost θ_v and q_v gradients. As discussed in detail in section 4d, the backing wind profiles associated with these “dry pockets” suggest that they may be associated both with the dryline and with misovortices propagating along the dryline.

d. Mobile sounding data

Horizontal gradients of boundary layer stratification are revealed by the mobile sounding array (Fig. 3). West of the primary dryline the hot, dry convective BL (CBL) is up to 300 mb deep with a nearly constant, well-mixed potential temperature and a slight decrease in mixing ratio with height (Fig. 3a,c). The CBL is capped by a warm dry layer around 600 mb (3.4 km AGL), approximately the LCL for a lowest 50-mb-average parcel. The winds west of the dryline are strong out of the south-southwest near the surface, veering slightly to southwest near the top of the CBL and subsequently veering to the west-southwest above the CBL. The sounding to the west of the minor dryline (Fig. 3a) is driest in the CBL. The water vapor mixing ratio remains nearly constant between 750 and 600 mb in the area between the primary and minor drylines (Fig. 3c), whereas to the west of the minor dryline this

layer dries rapidly with height (Fig. 3a). The lowest 750 m layer east of the dryline is relatively cool and moist with an LCL of 2.1 km (Fig. 3b), defining a shallow moist internal boundary layer.¹ The moist BL is capped by a warm, dry, elevated residual layer (ERL) created by advection of the dry CBL over the surface dryline location. The sounding in the ERL east of the dryline (Fig. 3b) is slightly cooler and moister than the sounding west of the dryline (Fig. 3b), implying some degree of mixing between the moist and dry BLs (Ziegler and Hane 1993).

e. Thermodynamic analyses

Surface water vapor mixing ratio fields from the Lagrangian analysis reveal aspects of dryline evolution (Fig. 10). The dryline is indicated as a sharply defined, undulating gradient in q_v residing in a narrow zone of confluence. The gradients reproduced by these analyses are on the order of 2–3 g kg⁻¹ km⁻¹, approximately the magnitude measured along each of the individual mobile mesonet dryline transects (Fig. 8). The nature of the analysis is such that the technique reproduces gradients (to be subsequently demonstrated in section 4a to form through frontogenesis) that are transported with the airflow to produce the analyzed surface structure. It will subsequently be shown in section 4d that a misocyclone may interact with the dryline to produce a low-amplitude dryline wave. Portions of the dryline periodically feature a band of drier air residing between the moist BL and a narrow moist tongue to the west (Figs. 10a,c). In these regions, the strongest confluence is located along the western moisture gradient, suggesting that the segmentation is a result of downward dry air entrainment on the moist side of the westernmost surface dryline segment (e.g., the 2344–2359 UTC P1 traverse, Fig. 8b). A minor dryline is located to the west of the primary dryline (Fig. 10a) early in the analysis period. Unlike the primary dryline, the moisture gradient associated with the minor dryline is much smaller (i.e., approximately 1–2 g kg⁻¹ km⁻¹). Fewer details in the structure of the minor dryline may be gleaned from this analysis, as it was only sampled by one mobile mesonet and the King Air.

A complex vacillating character of dryline movement is revealed by the 9-min interval Lagrangian analyses in the period 2242–0012 UTC (Fig. 11). At 2242 and 2251 UTC the dryline is located just west of X-Pol and Homestead and is moving very slowly westward, but by 2300 UTC the dryline has moved rapidly westward by several kilometers and becomes quasistationary. By

¹ An internal boundary layer is a shallow BL that displaces a deeper BL (Pielke 1984, p. 166).

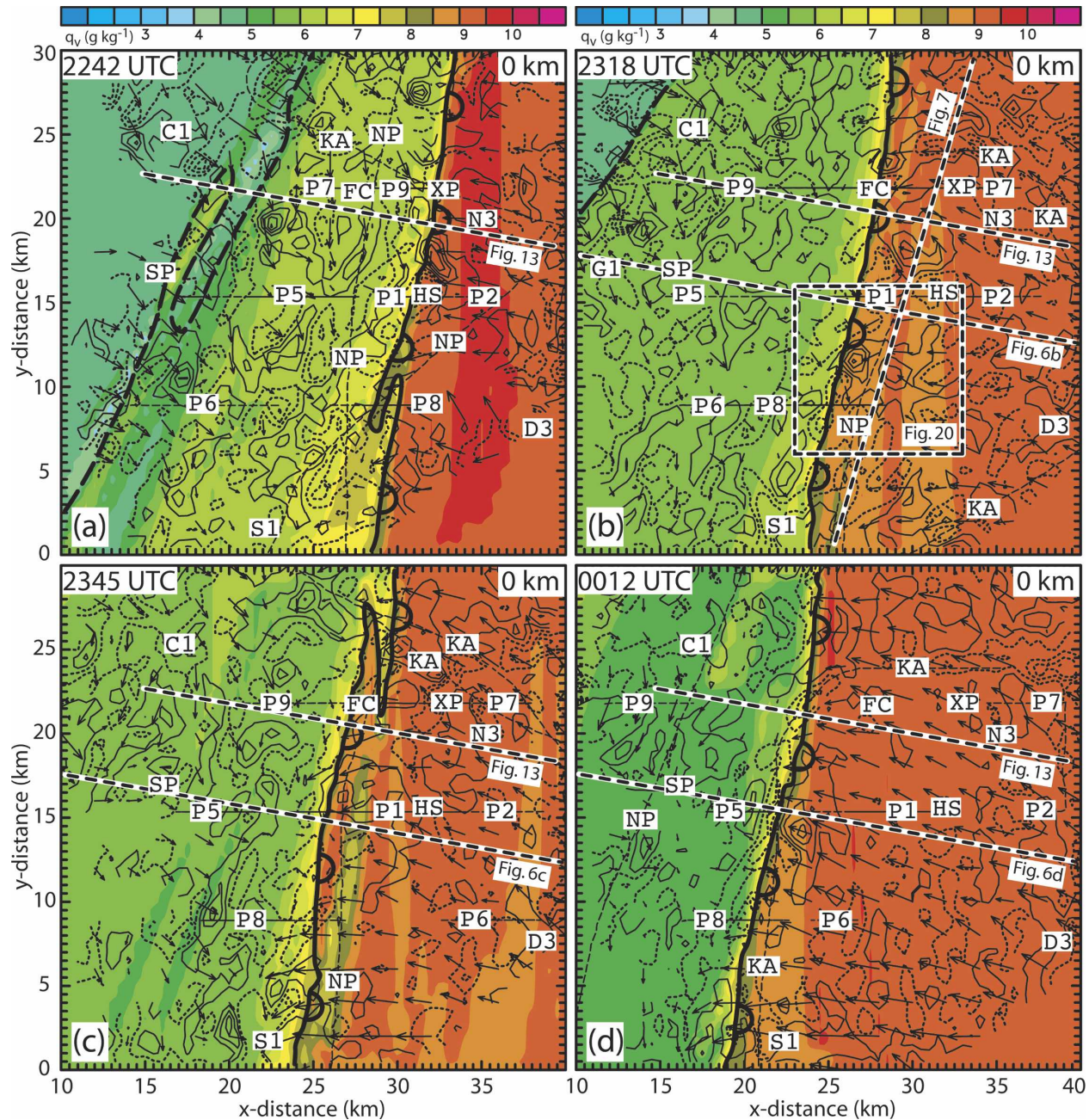


FIG. 10. Surface Lagrangian water vapor mixing ratio (g kg^{-1}) analysis on 22 May 2002. Horizontal misovortex-relative wind vectors (1-km length equal to 4 m s^{-1}) and vertical vorticity (s^{-1}) every $2 \times 10^{-3} \text{ s}^{-1}$ with positive values (black solid lines) starting at $1 \times 10^{-3} \text{ s}^{-1}$ and negative values (black dotted line) starting at $-1 \times 10^{-3} \text{ s}^{-1}$. The thin black lines and curves indicate various mobile mesonet and aircraft traverses. The thick scalloped line indicates the dryline and the thick dashed line indicates the minor dryline.

2327 UTC, the dryline has moved eastward and its southern portion is located at nearly the same position as it was at 2242 and 2251 UTC. Between 2327 and 2345 UTC, the dryline again moves westward before accelerating its retrogression between 2345 and 2354 UTC. From 2354 to 0012 UTC, the dryline continues its retrogression at varying speeds. Despite the vacillating

surface dryline position, the topography of the moist layer east of the dryline is characterized throughout the analysis period by its eastward-sloping interface with elevated drier air with increasing distance into the moist BL (Fig. 12). Northward deepening of the along-dryline moisture plume (Fig. 12) is caused by vertical advection in the dryline updraft relative to a strong

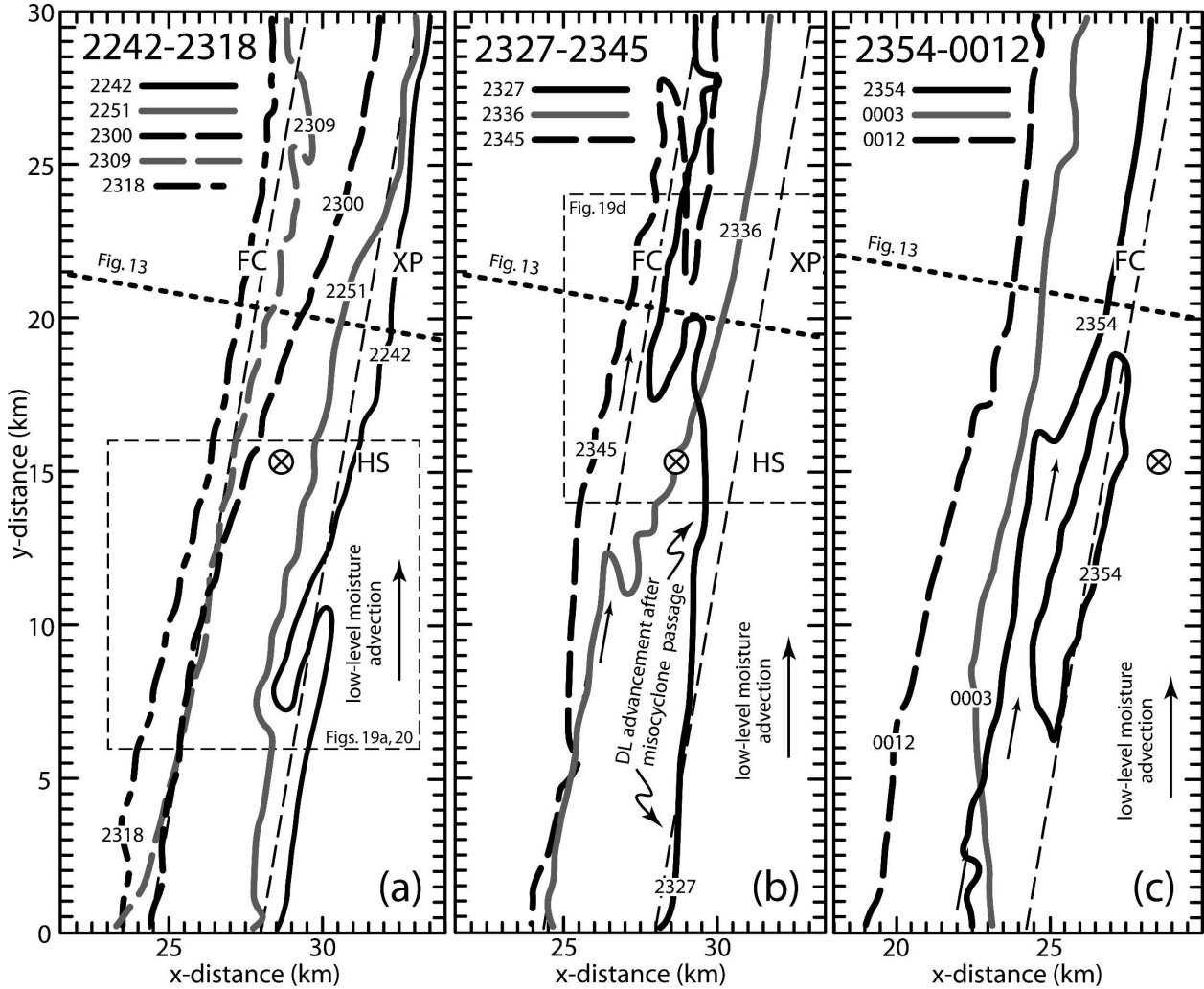


FIG. 11. Isochrones of the dryline as located by the 8 g kg^{-1} isohume at 9-min intervals from (left) 2242–2318 UTC, (middle) 2327–2345 UTC, and (right) 2354–0012 UTC obtained from the Lagrangian analyses on 22 May 2002. The circled X locates a profile site 3 km west of the Homestead (HS) profiler site that is referred to in the text. Thin dashed lines are fixed reference locations for tracking dryline positions.

meridionally oriented low-level jet. Moisture ridges in the moist BL top are suggestive of penetrative HCR circulations.

The most striking feature of the dryline-normal vertical BL structure is the strong and persistent secondary circulation, which produces a distinctive moisture and temperature plume structure at the dryline (Fig. 13). This vertical circulation and enhanced convergence, inferred to be forced by persistent solenoids in previous studies (e.g., Parsons et al. 1991; Ziegler et al. 1995), results in maximum updrafts consistently located around the dryline. These strong updrafts act to lift moisture at the head of the dryline, resulting in a local deepening of the moist layer. If the westerly shear is strong enough for moisture to exit the updraft, an elevated moist layer (Ziegler and Hane 1993) forms to

the east of the dryline (e.g., Fig. 13e). Additionally, the depth of the moist layer may be modulated by interactions with circulations in the ERL. Deeper moisture bands are oriented along the mean ERL flow, possibly assisted by the ascending branch of dry-side HCRs that are lifted up and over the dryline (Fig. 12), with clockwise reorientation of these elevated HCRs due to the solenoidally induced vertical shear. The compensating downward portion of the secondary circulation is locally strong enough to advect dry air from the ERL nearly to the surface just east of the dryline. It appears likely that downward transport of dry air in concert with subgrid-scale vertical mixing generates the segmented dryline structure described in section 3c. Relatively moist (dry) air is associated with relatively cool (warm) θ_v in the BL (i.e., left versus right columns of

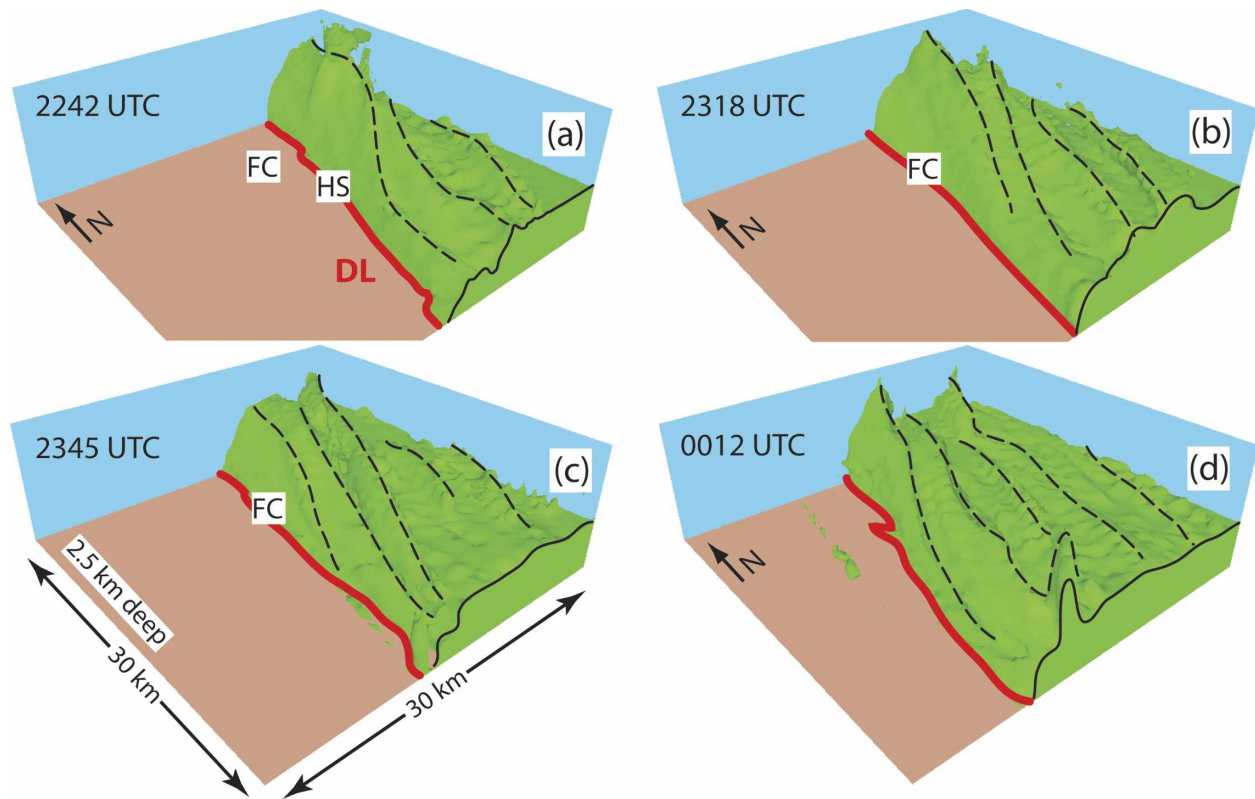


FIG. 12. 3D surfaces of the 6.7 g kg^{-1} water vapor mixing ratio value from the Lagrangian analyses at (a) 2242, (b) 2318, (c) 2345, (d) 0012 UTC. A solid red curve indicates the surface position of the dryline. A dashed black curve indicates a roll-like structure in the moist air, while a solid black curve locates the intersection of the southern lateral boundary with the moist BL.

Fig. 13). The high- q_v layer east of the dryline is quite shallow and is capped by the warm CBL air that is lifted and advected over the surface dryline. As with moisture, both the depth and structure of the θ_v field east of the dryline are modulated by roll circulations straddling the transition layer separating the BL and ERL. It will subsequently be shown in section 4b that the existence of θ_v (and therefore virtual density) gradients provide solenoidal forcing of the secondary circulation at the dryline.

Visible *Geostationary Operational Environmental Satellite-8 (GOES-8)* satellite images are analyzed on the radar grid at 2325 and 2345 UTC in relation to surface cloud photographs and the relative humidity field (Fig. 14). At 2325 UTC there are four main areas of cumulus clouds, two of which are along the dryline, one west of the dryline along an HCR, and one along the minor dryline (i.e., southwest of CAM1 location in Fig. 14a). In general these cumulus clouds are associated with updraft cores at the 1.5 km level. At 2345 UTC, the cumulus clouds have become concentrated along a band of higher vertical velocities at the dryline as the dryline circulation intensifies (Fig. 14b). Inspection of animated, time-lapse 90-s CAM1 cloud fields

(e.g., 2325 UTC image; Fig. 14c) and gridded *GOES-8* imagery reveal cloud areas moving from south to north across the domain and substantially evolving over a short (~ 10 min) period of time. The vertical dryline circulation brings air parcels from the moist and dry BLs into close proximity, providing conditions for mesoscale mixing (Ziegler and Hane 1993) and leading to strong relative humidity (RH) gradients (Figs. 14d,e). Although water saturation (i.e., cloud) is not achieved within the 2.5-km-deep analysis domain (Fig. 14d,e), the RH achieves local maximum values at 2.5 km at the observed cloud locations where mesoscale updrafts are lifting moisture toward the observed cloud bases at approximately 3.5–4 km AGL (Figs. 14d,e versus Figs. 14a–c).

Time–height cross sections of mixing ratio and virtual potential temperature reveal substantial heterogeneity in the BL around the Homestead profiler site (Fig. 15). Derived from the 9-min Lagrangian analyses of q_v and θ_v and the 3-min kinematic analyses of vertical motion and vorticity, the time–height cross sections are broadly comparable to the surface observations and time–height profiler analyses shown by Demoz et al. (2006).

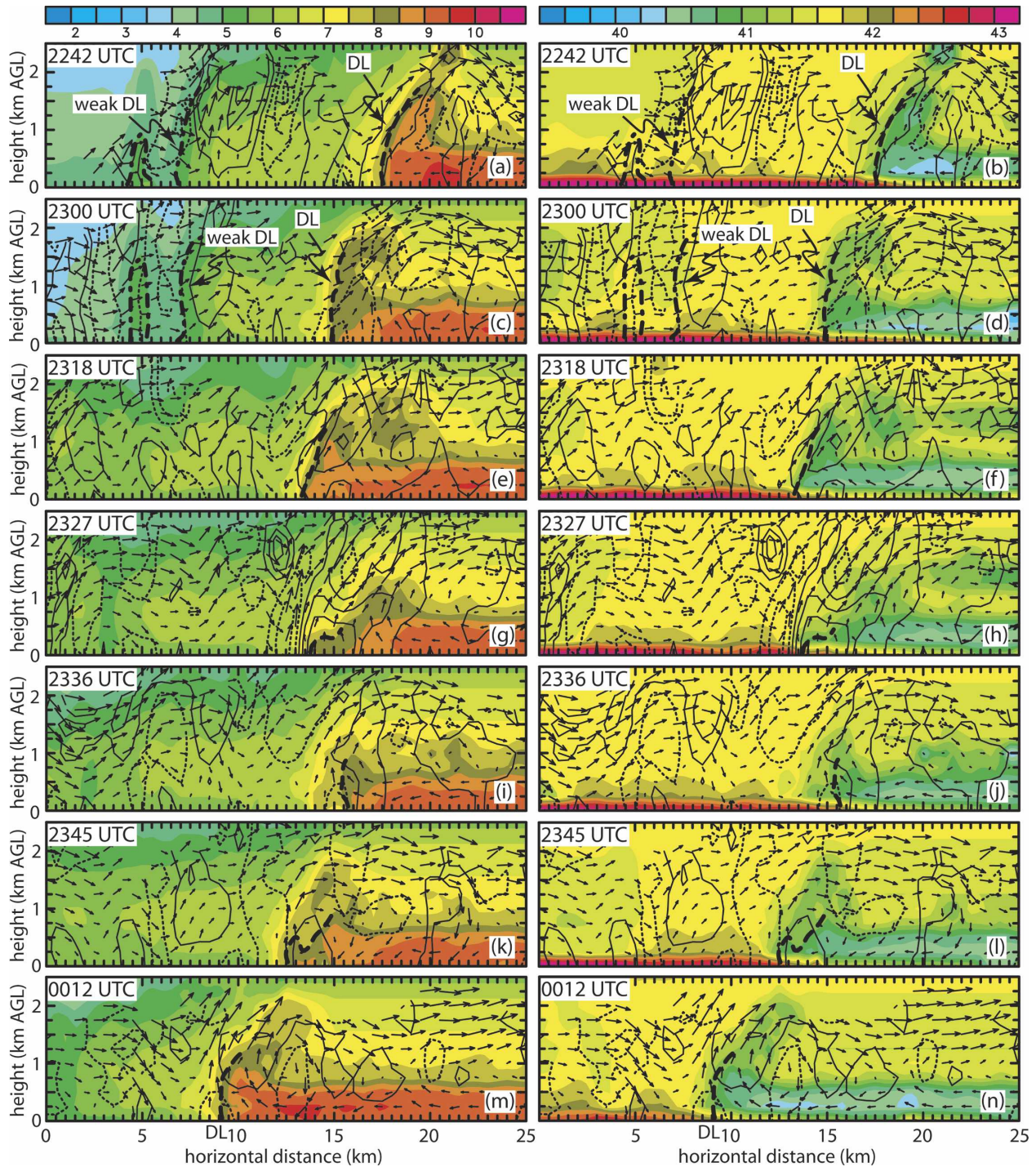


FIG. 13. Vertical cross sections of (left) water vapor mixing ratio (g kg^{-1}) and (right) virtual potential temperature (K). Ground-relative wind vectors (1-km length equal to 10 m s^{-1}), and vertical vorticity every $2 \times 10^{-3} \text{ s}^{-1}$ with positive values (black solid lines) starting at $1 \times 10^{-3} \text{ s}^{-1}$ and negative values (black dashed line) starting at $-1 \times 10^{-3} \text{ s}^{-1}$ are overlaid. The cross section location is shown in Fig. 10.

Except for a ~ 2 -min period around 2242 UTC in which the Homestead surface mesonet site at $(x, y) = (31.7, 15.3)$ experienced a transient cooling and drying (e.g., inset of Fig. 3 in Demoz et al. 2006), the Lagrangian

surface mixing ratio varies in the range of $8.5\text{--}9 \text{ g kg}^{-1}$ between 2242 and 0012 UTC (Fig. 15b) in good agreement with the fixed surface mesonet observations. As will be discussed further in section 4f, the transient sur-

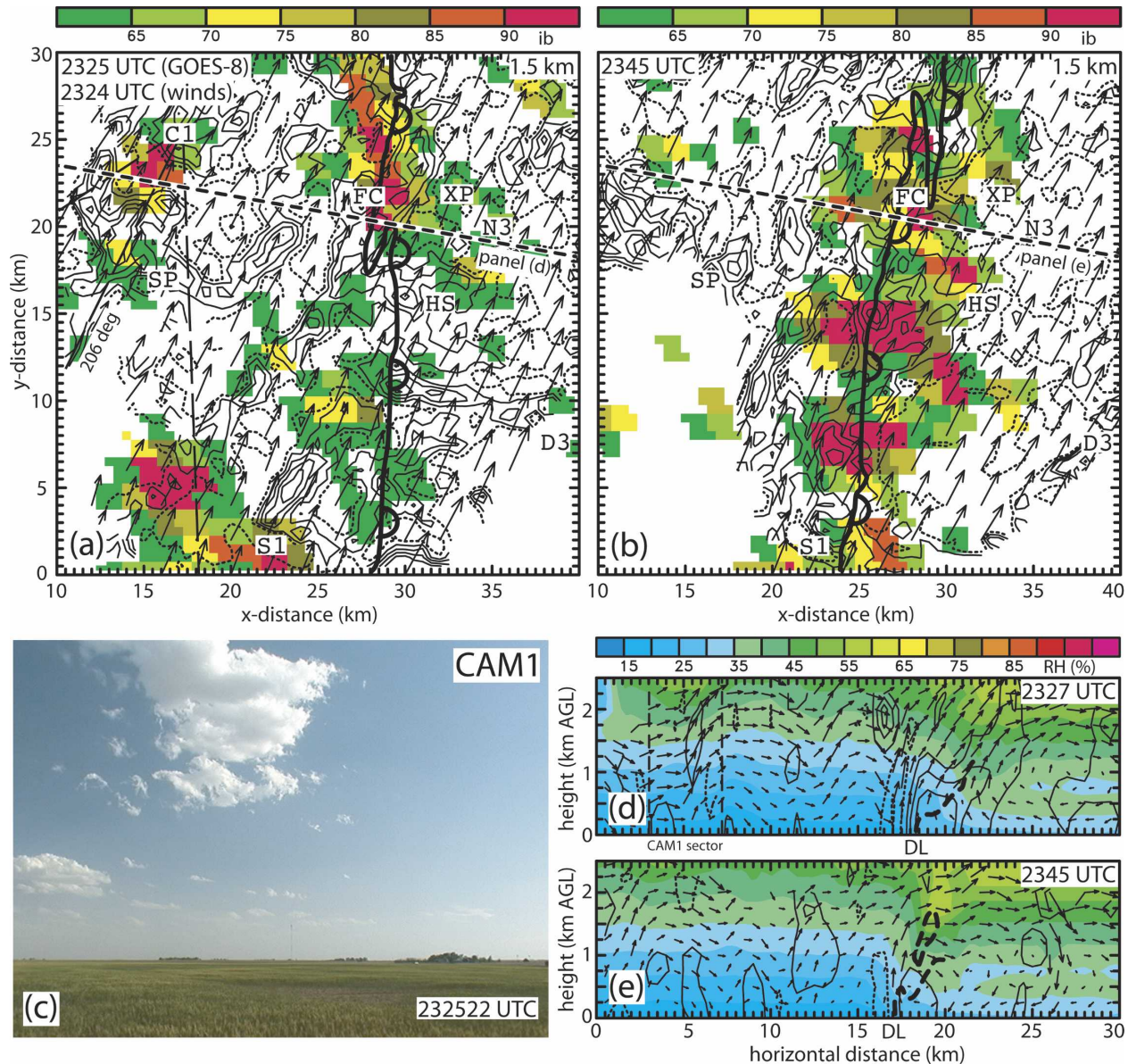


FIG. 14. GOES-8 visible satellite images at (a) 2325 and (b) 2345 UTC along with a ground-based camera view at (c) 2325 UTC and relative humidity (%) at (d) 2327 and (e) 2345 UTC 22 May 2002. Cross section locations in (d), (e) are indicated in (a), (b). GOES image brightness is color-filled on a scale of 0–255 with warmer colors identifying larger brightness values. Ground-relative horizontal wind ($1 \text{ km} = 10 \text{ m s}^{-1}$) and updraft (solid black curves every 1 m s^{-1} starting at 1 m s^{-1} , dotted line = zero contour) are shown in (a), (b) at 1.5 km. Vertical vorticity contours and vector velocity scaling in (d), (e) is as in Fig. 13.

face cooling and drying at Homestead around 2242 UTC may have been forced by BL downdrafts, which transported drier, cooler mid-BL air into the surface layer following the passage of a misocyclone detected by the radar analysis. Similar surface drying and cooling transients associated with possible dryline misocyclones were observed by P1 (Fig. 9a) and P8 (Fig. 9e), while P1 observed a sharply defined dryline with strong dryline-normal shear possibly supporting misocyclone development near the Homestead location (Fig. 9b). The

Homestead location is near the surface dryline position at 2242 and 2327 UTC and is east of the dryline during the remainder of the analysis period (Fig. 11). The aforementioned vacillation of surface dryline location results in rather strong local evolution of BL profiles just west of the Homestead profiler site (Figs. 15a,c). As the dryline moves slowly westward toward the selected location 3 km west of Homestead, its approximately 2D structure (e.g., Figs. 12–13) is manifested in a time-to-space conversion sense in the evolving q_v and

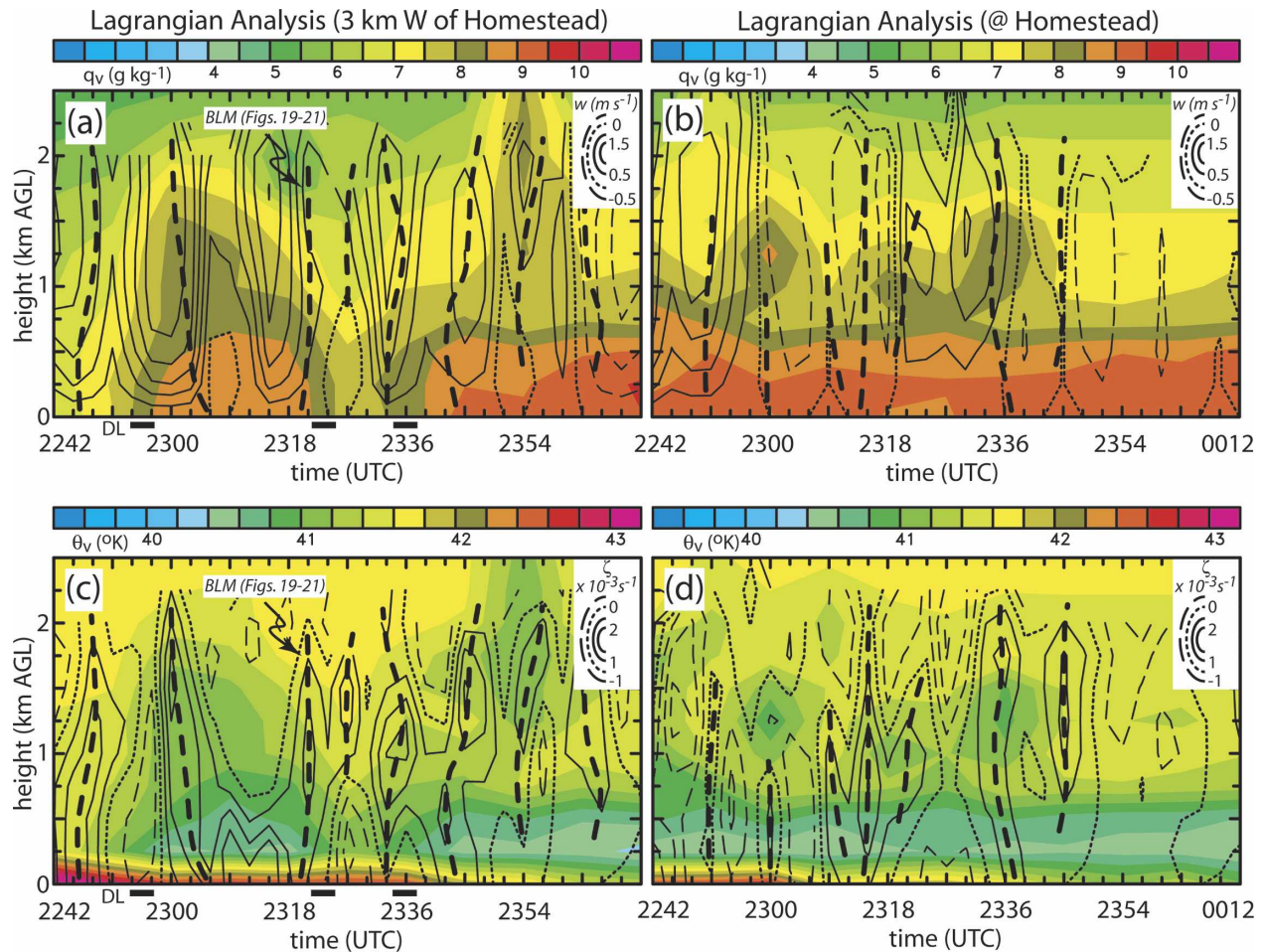


FIG. 15. Time–height cross sections taken at (b), (d) the Homestead location and (a), (c) 3 km west of Homestead. Mixing ratio is color filled at a 0.5 g kg^{-1} interval and vertical velocity is contoured every 1 m s^{-1} (top), while virtual potential temperature is color filled at a 0.2-K interval and vertical vorticity is contoured every $1 \times 10^{-3} \text{ s}^{-1}$ (bottom). The thick dashed black lines indicate locations of vortices.

θ_v profiles (Figs. 15a,c). An episode of abrupt drying and warming is noted around 2318 UTC as the dryline shifts to the east of the site. As the dryline resumes its retrograde motion after 2327 UTC (Fig. 11), the profiles again evolve from dry (hot) to moist (warm) conditions in a consistent sense with the 2D dryline structure and the westward dryline movement. Both a brief transient warming and drying in the ERL above 0.75 km and subsequently deeper BL moisture and cooler temperatures are associated with lifting of the across-dryline moisture and temperature gradients by the secondary dryline circulation around 2242–2300 UTC and again around 2318–2336 UTC when the dryline is just west of Homestead (Figs. 15b,d).

The depth of BL moisture evolves as updrafts lift BL moisture into the ERL or as downdrafts entrain dry air into the moist BL (Figs. 15a,b), a vertical mesoscale transport and mixing process that is consistent with the

SRL profiler observations (e.g., Figs. 9 and 13 of Demoz et al. 2006). Typical of strongly mixed conditions in the CBL (e.g., Betts 1984), the θ_v and q_v field values are negatively correlated due to upward transport of relatively cool, moist air in updrafts and downward transport of relatively warm, dry air in downdrafts (i.e., resolved-scale transport plus smoothing, which is analogous to subgrid mixing). The θ_v in the lowest $\sim 100 \text{ m}$ gradually decreases with time as the dryline retrogrades to the west due to the dryline-relative east–west θ_v gradient, and cooling is enhanced by the loss of surface heating in the early evening (Figs. 15c,d). Subsequent weakening of the superadiabatic layer near the surface associates with decreasing vertical vorticity values in the moist BL. It is speculated that this decreasing enstrophy is due to elimination of thermally forced turbulence as the surface heat flux vanishes (e.g., André et al. 1978; Weckwerth et al. 1997; Kanak et al. 2000). It is

interesting to note that enstrophy is observed to persist in the nearly neutral ERL at the same time as BL values are decreasing, suggesting that remnants of thermally forced turbulent elements that arose west of the dryline persist after moving to the east of the surface dryline location.

4. Discussion

a. Dryline frontogenesis

Frontogenesis produces and maintains across-dryline thermal and moisture gradients. Koch and McCarthy (1982) calculated the horizontal component of frontogenesis from a mesonetwork of surface stations and found that frontogenesis near the surface contributed to the intensification of the dryline. Using a simple 3D model, Anthes et al. (1982) found that frontogenesis contributed to the dryline formation on the regional scale. Ziegler et al. (1995) used a 2D model with a 5-km horizontal grid spacing to show the vertical structure of frontogenesis perpendicular to the dryline. In the present study, the structure of the frontogenesis field can be diagnosed both in 4D and on much smaller scales than previously reported.

The horizontal frontogenesis of q_v is calculated to diagnose regions where moisture gradients are being increased or decreased along the dryline (Fig. 16). Neglecting source, sink, and mixing terms and considering only horizontal components in the full three-dimensional frontogenesis equation (Bluestein 1993), the two-dimensional form of the equation can be expressed as

$$F = \frac{1}{|\nabla_h q_v|} \left[\frac{\partial q_v}{\partial x} \left(-\frac{\partial u}{\partial x} \frac{\partial q_v}{\partial x} - \frac{\partial v}{\partial x} \frac{\partial q_v}{\partial y} \right) + \frac{\partial q_v}{\partial y} \left(-\frac{\partial u}{\partial y} \frac{\partial q_v}{\partial x} - \frac{\partial v}{\partial y} \frac{\partial q_v}{\partial y} \right) \right], \quad (1)$$

where $\nabla_h = (\partial/\partial x)\mathbf{i} + (\partial/\partial y)\mathbf{j}$. The surface dryline is primarily frontogenetic along its length, except for a few locations with varying frontolysis strength (Fig. 16). Along-dryline gradients are advected and also strengthened in the downstream direction, because airflow trajectories are nearly parallel to the dryline and thus experience confluent forcing over long residence times within the dryline zone. The minor dryline is also predominantly frontogenetic, but the magnitude is generally less than that of the primary dryline due to the weaker values of confluence and moisture gradient.

The dryline zone exhibits frontogenesis at low levels and frontolysis at higher levels (Fig. 17), indicative of strong convergence in the lower part and divergence in the upper part of the BL along the dryline (Ziegler et al. 1995). As air is lifted in the updraft, the strong sec-

ondary circulation rotates the large horizontal across-dryline moisture gradients into vertical gradients (i.e., stratification). This process of lifting and rotating surface horizontal gradients is frontolytic in the 2D horizontal planes in which the frontogenesis function is calculated. The structure of the frontogenesis along the minor dryline is similar to that along the primary dryline, with frontogenesis (frontolysis) at lower (upper) levels of the BL.

b. Vorticity dynamics of the mesoscale secondary circulation at the dryline

Previous modeling studies have suggested that solenoidal forcing is the primary mechanism for vorticity generation within the secondary circulation (Sun and Ogura 1979; Sun and Wu 1992; Ziegler et al. 1995). These studies, however, used grid spacings much larger than the horizontal scale of the maximum possible dryline gradients. In the present study, terms in the vorticity equation can be computed both on the scale of the dryline gradients and in 3D using the Lagrangian analyses.

Several terms in the vorticity equation were computed to diagnose the primary forcing leading to the generation of the secondary circulation normal to the dryline. Using the Exner function π as the pressure variable, substituting the ideal gas law for moist air, and linearizing terms involving q_v and π while considering the special case of zero hydrometeor loading, the 3D equation of motion can be written as (Houze 1993)

$$\frac{D\mathbf{v}}{Dt} = -c_p \bar{\theta}_v \nabla \pi' - f \mathbf{k} \times \mathbf{v} + g \left(\frac{\theta'_v}{\bar{\theta}_v} \right) \mathbf{k} + \mathbf{F}. \quad (2)$$

Here c_p is the specific heat at constant pressure, f is the Coriolis parameter, g is the gravitational acceleration, \mathbf{F} is the friction force, primes and overbars denote perturbation and mean quantities respectively. Taking the curl of (2), the horizontal components of the vorticity equation take the form

$$\begin{aligned} \frac{D\xi}{Dt} = & \left(\frac{\partial v}{\partial x} \frac{\partial u}{\partial z} - \frac{\partial w}{\partial x} \frac{\partial u}{\partial y} \right) - \xi \left(\frac{\partial v}{\partial y} + \frac{\partial w}{\partial z} \right) + c_p \frac{\partial \theta_{v_0}}{\partial z} \frac{\partial \pi'}{\partial y} \\ & + \frac{g}{\theta_{v_0}} \frac{\partial \theta'_v}{\partial y} + f \frac{\partial u}{\partial z} + \left(\frac{\partial F_z}{\partial y} - \frac{\partial F_y}{\partial z} \right) \end{aligned} \quad (3)$$

and

$$\begin{aligned} \frac{D\eta}{Dt} = & \left(\frac{\partial w}{\partial y} \frac{\partial v}{\partial x} - \frac{\partial u}{\partial y} \frac{\partial v}{\partial z} \right) - \eta \left(\frac{\partial u}{\partial x} + \frac{\partial w}{\partial z} \right) - c_p \frac{\partial \theta_{v_0}}{\partial z} \frac{\partial \pi'}{\partial x} \\ & - \frac{g}{\theta_{v_0}} \frac{\partial \theta'_v}{\partial x} + f \frac{\partial v}{\partial z} + \left(\frac{\partial F_z}{\partial y} - \frac{\partial F_y}{\partial z} \right), \end{aligned} \quad (4)$$

where ξ and η are the components of vorticity in the x and y directions, respectively. The rhs terms (from left

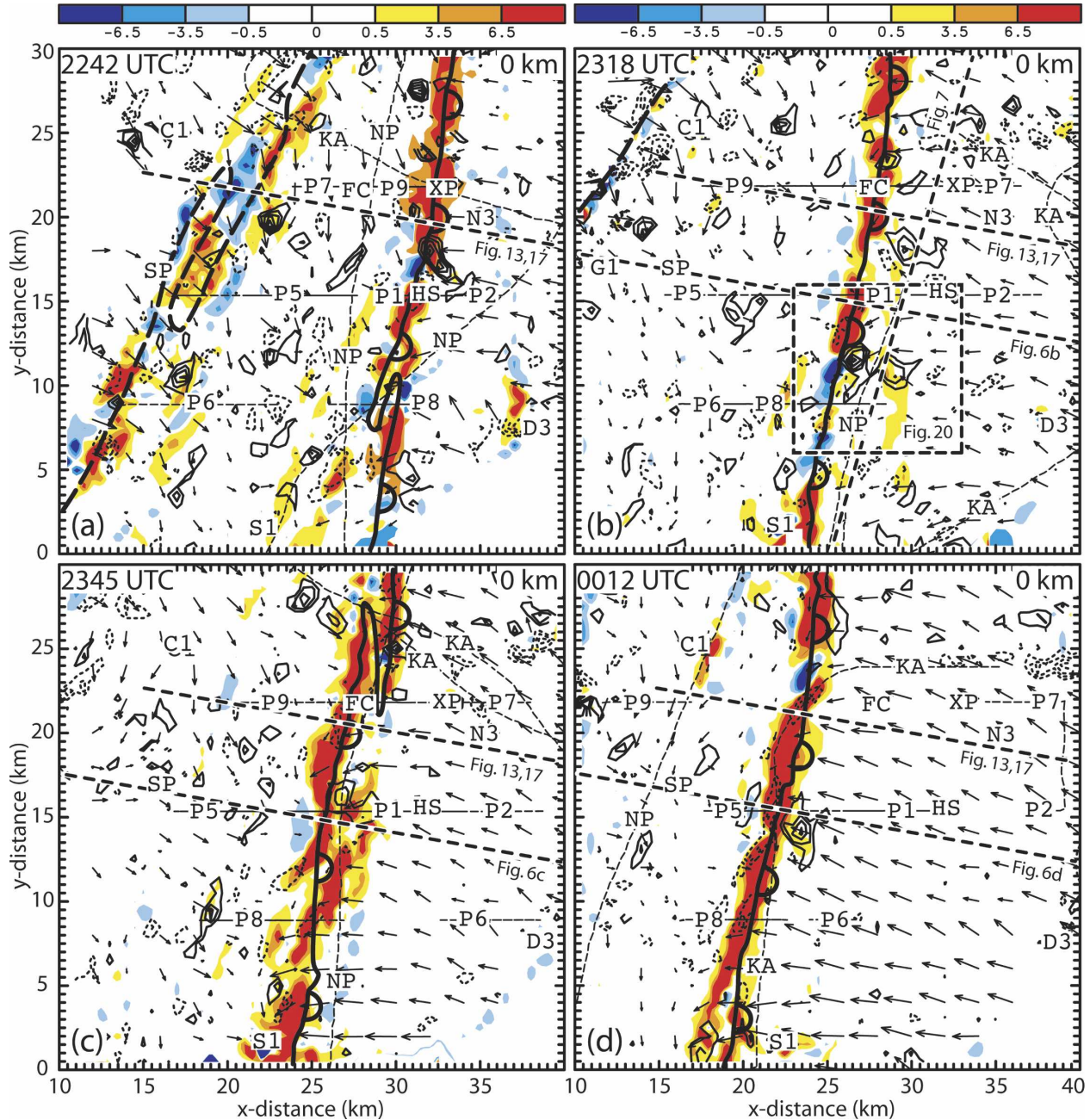


FIG. 16. 2D horizontal frontogenesis ($\times 10^6 \text{ g kg}^{-1} \text{ s}^{-1} \text{ m}^{-1}$) of water vapor mixing ratio (color filled), misovortex-relative horizontal wind vectors ($1 \text{ km} = 4 \text{ m s}^{-1}$), and vertical vorticity every $2 \times 10^{-3} \text{ s}^{-1}$ with positive values (black solid lines) starting at $3 \times 10^{-3} \text{ s}^{-1}$ and negative values (black dashed line) starting at $-3 \times 10^{-3} \text{ s}^{-1}$. The thin black lines indicate mobile mesonet and aircraft traverses.

to right) are the tilting, stretching, perturbation pressure solenoid, buoyancy solenoid, earth-spin vorticity tilting, and frictional tendencies. The perturbation pressure solenoid term is not computed in the present study, as it has been shown to be two orders of magnitude smaller than the buoyancy solenoid term in similar dryline environments (Ziegler et al. 1995). The frictional term was also neglected as this term is expected

to be a small sink term compared with the dominant solenoidal source term. To compare the relative magnitudes of the forcing terms on the scale of the secondary circulation, the mean and standard deviation values of each term were computed at 0.25 km within a 10 km long by 5 km wide area centered on the dryline secondary circulation.

Although extreme values of the buoyancy solenoid,

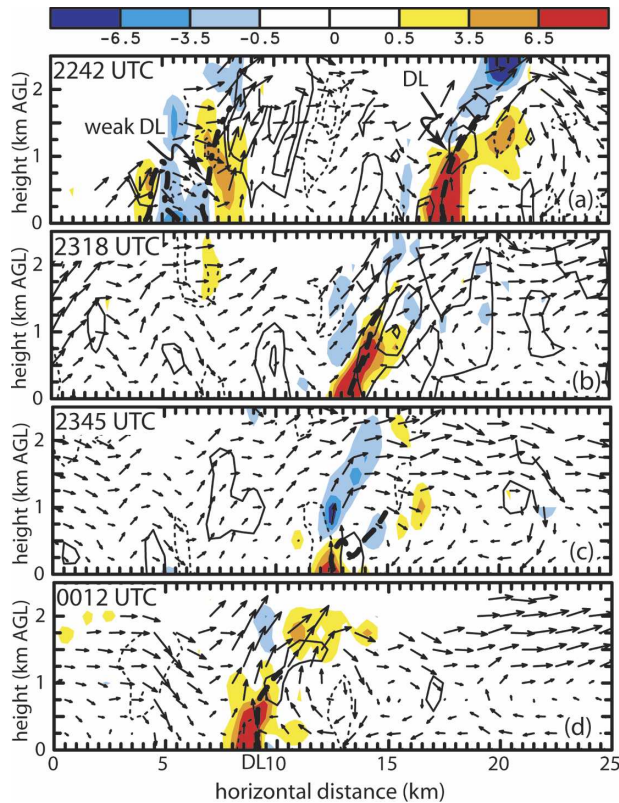


FIG. 17. Vertical cross section of 2D horizontal frontogenesis ($\times 10^6 \text{ g kg}^{-1} \text{ s}^{-1} \text{ m}^{-1}$) of water vapor mixing ratio (color filled), ground-relative wind vectors ($1 \text{ km} = 10 \text{ m s}^{-1}$), and vertical vorticity every $2 \times 10^{-3} \text{ s}^{-1}$ with positive values (black solid lines) starting at $2 \times 10^{-3} \text{ s}^{-1}$ and negative values (black dashed line) starting at $-2 \times 10^{-3} \text{ s}^{-1}$. Cross section locations are shown by the dashed black lines in Fig. 16. The dashed black lines indicate dryline locations.

stretching, and tilting terms are on the same order of magnitude, as seen by summing the means and the standard deviations (Table 4), plots of the three terms (not shown) indicate that the stretching and tilting terms have a smaller scale structure (i.e., $\sim 1 \text{ km}$) than the solenoid term. The secondary circulation is primarily

forced by the buoyancy solenoid, confirming and extending the 2D modeling results of Ziegler et al. (1995). The tilting term contributes considerably less, while the stretching term actually opposes the secondary circulation due to longitudinal compression of streamwise vortex tubes entering the dryline updraft bands.

The dryline-normal secondary circulation is forced by a persistent positive solenoidal contribution within the dryline zone, with the strongest forcing residing in the lower levels toward the warm (western) side of the circulation (Fig. 18). The solenoidal forcing acts to enhance the dryline updraft and generate westerly shear over the moist layer. The solenoidal forcing reverses sign on the eastern flank of the dryline updraft as cooler θ_v air is lofted by the penetrative circulation (e.g., right column of Fig. 13). Smaller pockets of alternating-sign of solenoidal forcing also develop along the interface of the moist layer and overlaying ERL due to the effects of roll circulations (Fig. 18).

c. Roll dynamics

Theoretically, the two forcing mechanisms thought to lead to roll formation are thermal instability and dynamic instability. In the case of thermal instability the CBL typically contains variable surface layer heat flux and is convectively unstable in low levels. An HCR obtains energy through buoyancy while the boundary layer wind shear acts to organize the convection (Weckwerth et al. 1997). Dynamic instability may take the form of parallel instability (e.g., Lilly 1966; Shirer 1986) or inflection point instability (e.g., Brown 1980; Brümmer 1985). With parallel instability the roll energy is obtained through the along-roll shear component, whereas in the case of inflection point instability the roll energy is extracted from the component of the sheared flow normal to the roll axis (Stensrud and Shirer 1988). Typically, however, combinations of both types of instability are often found when rolls are observed (Gossard and Moninger 1975). The transverse

TABLE 4. Average values of the buoyancy solenoid, stretching, tilting, and Coriolis terms of the vorticity equation (units: $\times 10^6 \text{ s}^{-2}$) computed at 0.25 km AGL at each of the 11 analysis times, with the standard deviation of each term in parenthesis.

Analysis time	Solenoidal	Stretching	Tilting	Coriolis
2242 UTC	4.67 (5.41)	-1.78 (13.00)	-0.22 (5.99)	0.02 (0.11)
2251 UTC	5.21 (4.17)	-1.70 (7.21)	0.06 (4.20)	0.02 (0.08)
2300 UTC	4.74 (6.67)	-2.52 (8.54)	-0.01 (3.83)	-0.02 (0.10)
2309 UTC	5.76 (5.90)	-0.92 (8.84)	0.40 (4.43)	0.01 (0.10)
2318 UTC	5.59 (4.97)	-0.31 (6.12)	-0.02 (4.16)	0.01 (0.10)
2327 UTC	5.26 (5.05)	-1.95 (4.23)	-0.03 (3.11)	0.00 (0.09)
2336 UTC	5.06 (4.18)	-1.98 (7.63)	0.17 (3.23)	0.00 (0.10)
2345 UTC	5.42 (4.99)	-2.41 (5.69)	0.62 (2.75)	0.01 (0.08)
2354 UTC	4.87 (6.24)	-2.59 (10.57)	0.64 (3.71)	-0.01 (0.09)
0003 UTC	6.12 (8.96)	-1.66 (7.81)	0.36 (4.30)	-0.04 (0.13)
0012 UTC	4.58 (8.39)	-0.81 (7.60)	-0.16 (4.74)	-0.06 (0.13)

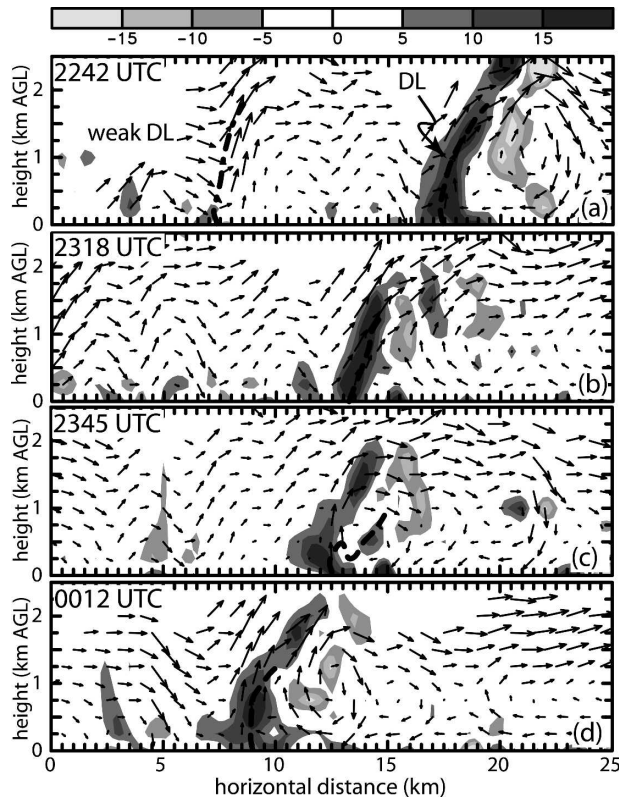


FIG. 18. Vertical cross section of the horizontal, plane-normal component of solenoidal vorticity generation ($\times 10^6 \text{ s}^{-2}$) due to the buoyancy term (shaded). Ground-relative wind vectors are scaled with $1 \text{ km} = 10 \text{ m s}^{-1}$. Cross section locations are the same as in Fig. 17. The dashed black lines indicate dryline locations.

rolls discussed in section 3b (Figs. 5, 7) appear to be consistent with an inflection point instability.

An inflection point instability was identified in the ERL between 0.75 and 2.5 km based on the mean horizontal radar wind analysis profiles in the area where the rolls were observed (i.e., east of the dryline) using the Stensrud and Shirer model (Stensrud and Shirer 1988). The inflection point in this layer was confirmed by a sounding obtained by the Wyoming King Air as it ascended through the BL around the southeast corner of the radar analysis domain just after 0000 UTC. For the layer between 0.75 and 2.5 km, the angle of the most-unstable inflection point instability mode was predicted to be 286° , which is consistent with the orientation of the observed rolls (Fig. 5). Note that the cross sections in Fig. 7 were oriented normal to the azimuth of the most unstable mode for reference.

To assess the alternative possibility that the transverse circulations east of the dryline are consistent with gravity waves, the theoretical gravity wave phase speed was computed from the observations and compared to the roll's motion. As the inversion at the top of the

internal BL is very shallow, a two-layer model can be used. For gravity waves at the interface of two fluids of differing density, the phase speed relative to the flow is $c = \pm(1/k)(\sqrt{gk(\theta_2 - \theta_1)/(\theta_2 + \theta_1)})$, where k is the horizontal wavenumber ($k = 2\pi/L$ and L is the horizontal wavelength), g is the gravitational acceleration, and θ_1 and θ_2 are the potential temperatures of the lower and upper layer, respectively (Kundu 2002). Soundings were used to determine potential temperatures of the two layers ($\theta_1 = 311.8 \text{ K}$ and $\theta_2 = 313.2 \text{ K}$). The value of k was determined using the observed value $L = 5 \text{ km}$ from the radar analyses, and the phase speed was computed as $\pm 4.2 \text{ m s}^{-1}$ relative to the BL flow. Because the radar-observed transverse circulations move with the BL flow, they do not appear to be a manifestation of gravity waves.

d. Interactions between rolls, the dryline, and misocyclones

Pietrycha and Rasmussen (2004) showed several cases where small-scale vortices were observed to track and both augment and rotate the moisture gradients along the dryline. Marquis et al. (2007) observed misocyclones along boundaries on 3 days during IHOP. Vortex–dryline interactions and misocyclone structure in the present case are broadly similar to those aspects of the Pietrycha and Rasmussen (2004) and Marquis et al. (2007) studies. The presence of misocyclones along boundaries is important because they are believed to influence CI by augmenting the moisture and convergence fields. Given the high-resolution Lagrangian and radar analyses, the structure of dryline misocyclones and their effect on the kinematic and thermodynamic fields may be interpreted to improve the understanding of CI processes.

The radar analyses are examined to find examples of misocyclones along the dryline (e.g., Marquis et al. 2007), and three particularly intense dryline misocyclones with very similar morphology and evolution were identified. In a series of radar analyses presented in a reference frame following the motion of the strongest of the three dryline misocyclones (i.e., the misocyclone located in the dashed box in Fig. 5b), an undulation of the dryline updraft moves northward with the misocyclone remaining located near its inflection point (Fig. 19). The misocyclone is located near the intersections of the dryline with a longitudinal HCR extending upstream into the dry air and a transverse roll extending into the moist air (see also Fig. 5b). Both the dryline and the misocyclone, the latter with a maximum vertical vorticity of $9 \times 10^{-3} \text{ s}^{-1}$, show remarkably little evolution over 9 min.

The enhanced Lagrangian analysis described in sec-

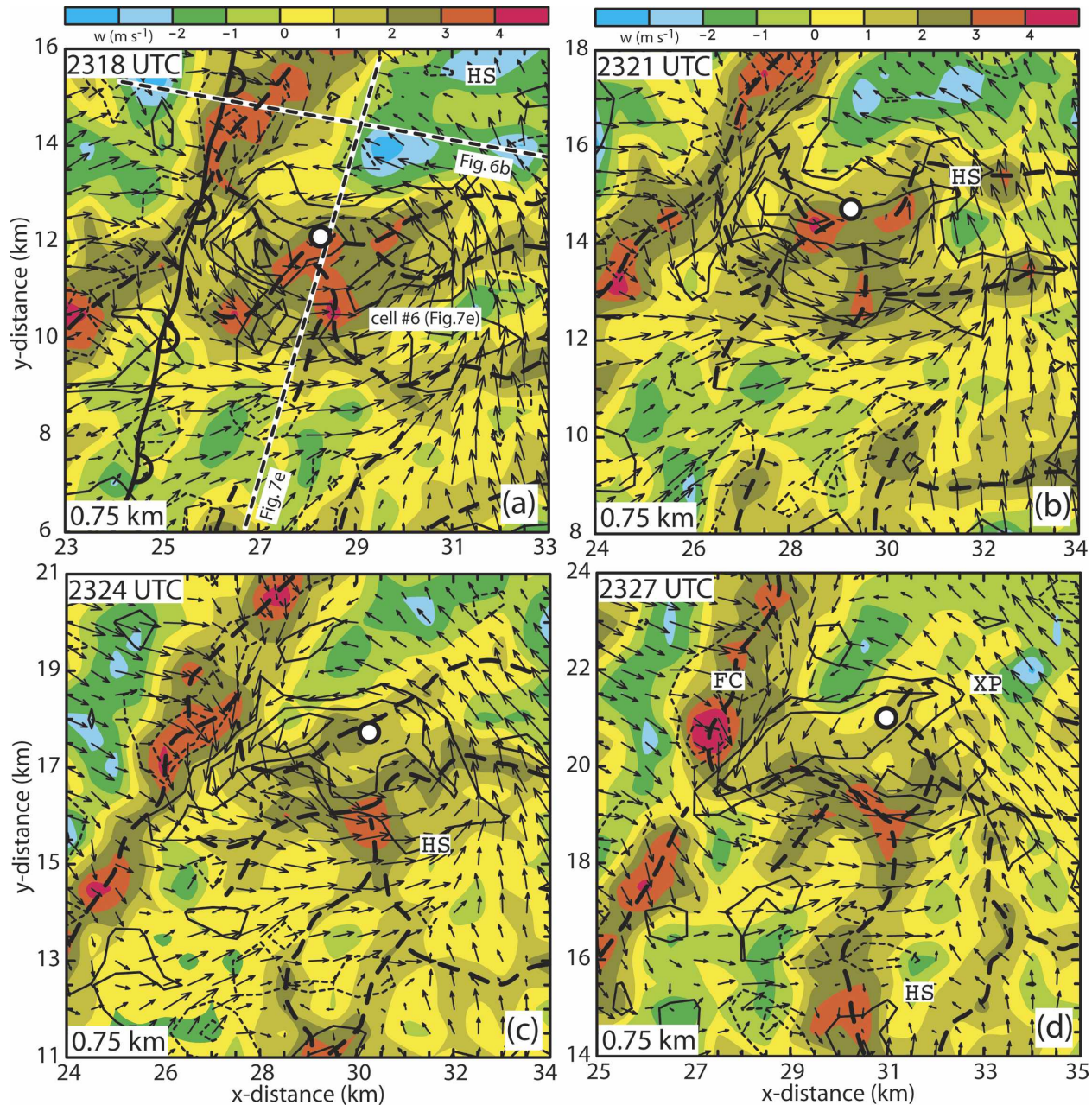


FIG. 19. Misovortex-relative horizontal velocity (vectors) and vertical velocity (color filled) in a misocyclone-following subdomain, with vectors plotted every grid point and negative (dotted line) and positive (solid line) vertical vorticity contoured every 2×10^{-3} starting at 2×10^{-3} : (a) 2318, (b) 2321, (c) 2324, (d) 2327 UTC. The white circle with black outline indicates the center of the vortex at each time. The thick dashed black lines denote updraft bands. The location of the grid at 2318 UTC is shown in Fig. 5b.

tion 2c has been applied in the misocyclone-following subdomain to elucidate the detailed thermal and moisture structure of the vortex. The dryline moisture gradient displays an inflection or S-shape similar to the updraft pattern (Fig. 20). The misocyclonic circulation induces westward (eastward) advection of moist (dry) air, thus rotating a segment of the dryline counterclockwise from a north–south toward an east–west orienta-

tion and forcing an inflection of the dryline (Fig. 20a). A similar stair-step profile of convergence and reflectivity was found near misocyclones along several other IHOP boundaries by Marquis et al. (2007). Low-level BL moisture rises cyclonically and eventually processes around the western and southern edges of the misocyclone around 1 km (Fig. 20b). The misocyclone also entrains drier air along the southern edge of the circu-

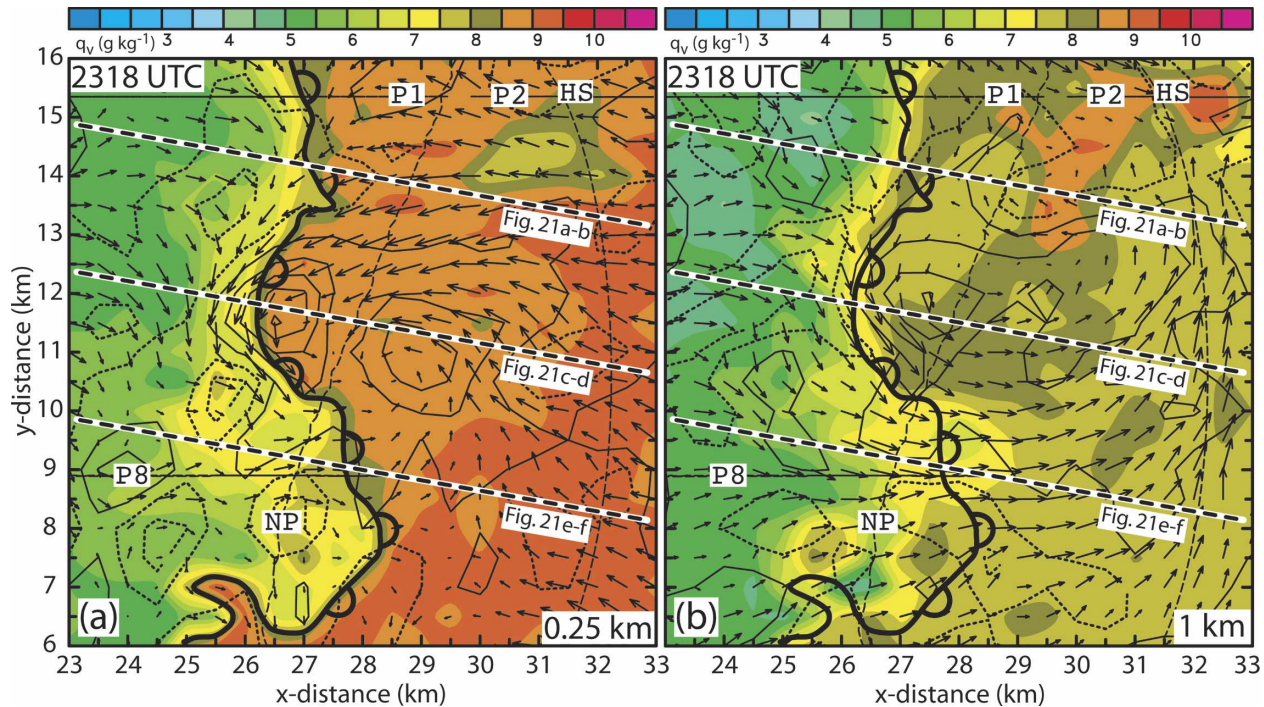


FIG. 20. Water vapor mixing ratio (color filled), horizontal vortex-relative winds (vectors), and vertical vorticity at (a) 0.25 and (b) 1 km at 2318 UTC 22 May 2002. Vectors are scaled with $1 \text{ km} = 10 \text{ m s}^{-1}$. Vertical vorticity contours are dotted (negative) or solid (positive) curves at a $2 \times 10^{-3} \text{ s}^{-1}$ interval starting at -1×10^{-3} and $1 \times 10^{-3} \text{ s}^{-1}$, respectively. The locations of each grid are the same as in Fig. 23, with (a) located as in Fig. 10b. The surface dryline locations are shown by the solid scalloped curve.

lation at 1 km (Fig. 20b), generating a strong moisture gradient along the south flank of the misocyclone.

The effect of the misocyclone’s 3D airflow on moisture transport and dryline position is further examined in vertical cross sections of the enhanced Lagrangian analysis relative to the path and location of the vortex (Fig. 21). To the north of the vortex at 2318 UTC, deep easterly flow transports moisture westward relative to the vortex, thereby locally deepening the moist layer while assisting dryline frontogenesis (Fig. 21a). Moisture upwelling in the center of the vortex is tilted eastward due to westerly shear (Fig. 21c). To the south of the vortex, the westerly flow brings dry air eastward and, combined with mesoscale mixing, rapidly decreases the depth of the moist layer and weakens the western dryline segment (Fig. 21e). Convergent frontogenesis strengthens both the western and eastern drylines located to the north and south of the misocyclone, respectively (Figs. 16b, 21e). The reflectivity structure follows a similar pattern to that of the vertical velocity and moisture, as the boundary layer scatterers are concentrated in updraft cores and diluted by mixing following dryline passage (Figs. 21b,d,f).

A conceptual model was developed from the analyses of the three strongest misocyclones to illustrate the vorticity interaction of the BL rolls with an embedded

misocyclone and the dryline (Fig. 22). Vortex lines were computed from wind analyses and a composite was used to create the conceptual vortex tube orientations. Hypothetically, an HCR originating in the dry BL west of the dryline interacts with the dryline secondary circulation and is tilted into the vertical (Fig. 22, roll A). As the horizontal streamwise vorticity associated with the HCR (i.e., roll A) is tilted vertically and stretched by the dryline updraft, the misocyclone develops. The vortex tube associated with roll A then exits the misocyclone, is tilted downward and compressed, and continues along a constant orientation. Transverse rolls east of the dryline (roll D) may enhance vertical motion along the dryline, modulating the vortex lines associated with the HCR. Misocyclone strengthening (weakening) may also occur when the misocyclone and transverse roll updrafts are in (out of) phase. Vortex lines east of the dryline (roll C) are tilted vertically and are stretched on the eastern side of the misocyclone. Near the center of the misocyclone (roll B), vortex lines arise from very low levels, perhaps emanating from a descending HCR branch in a downdraft that subsequently tilts upward in the adjacent misocyclonic updraft. Additionally, horizontal vorticity oriented at right angles to the low-level shear at very low levels within the friction layer may be tilted vertically by the misocyclone

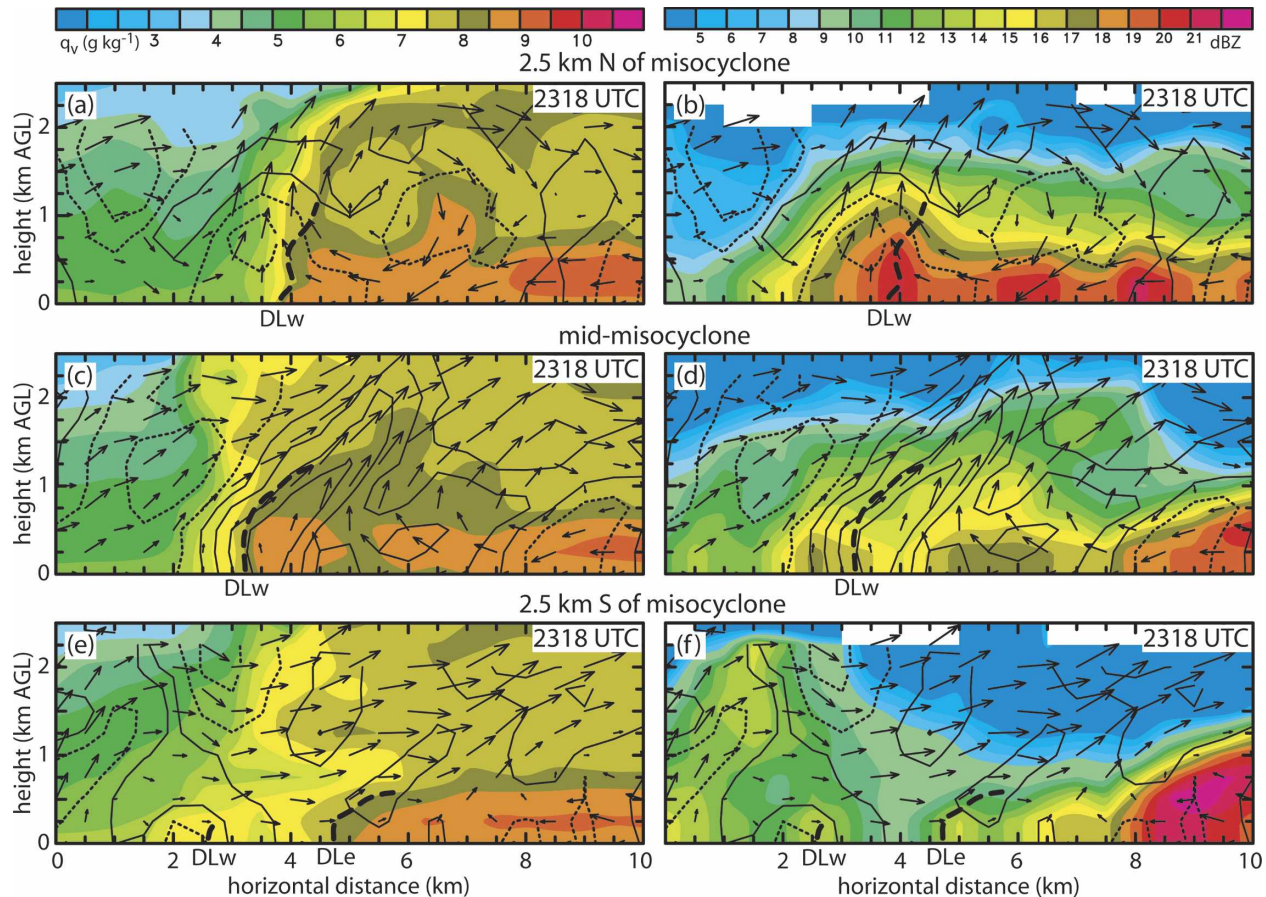


FIG. 21. Radar and Lagrangian analysis fields at 2318 UTC 22 May 2002. (left) Vertical cross sections of q_v (g kg^{-1}); (right) reflectivity (dBZ). Negative (dotted line) and positive (solid line) vertical vorticity is contoured every $2 \times 10^{-3} \text{ s}^{-1}$ starting at $1 (-1) \times 10^{-3} \text{ s}^{-1}$, while wind vectors are scaled with $1 \text{ km} = 6 \text{ m s}^{-1}$. The cross sections are 2.5 km north of the vortex (top), through the vortex (middle), and 2.5 km south of the vortex (bottom) as indicated in Fig. 20.

updraft to further enhance roll B. As the misocyclone develops, its advection of moisture would be expected to move the dryline westward to the north and eastward to the south of the vortex. Frontogenesis both northwest and southeast of the misocyclone strengthen the dryline gradients at those locations (see inset box, Fig. 16b). The overall dryline misovortex-relative frontogenesis pattern is similar to analytical fields calculated for a nondivergent vortex acting on an initially linear gradient zone (Doswell 1985).

e. Validating Lagrangian analysis with S-Pol refractivity-derived moisture fields

Because the near-surface moisture observations are sparse compared with the scales believed to be important for CI, Fabry et al. (1997) developed a technique to extract small-scale moisture information using radar refractivity. To validate this technique, the present study

compares refractivity-based moisture fields with the independent moisture fields based on Lagrangian analysis of in situ observations. Because low-level moisture is of primary importance to the development and maintenance of convection, knowledge of the moisture structure on the cloud-scale is essential to improving thunderstorm forecasts. A provision of estimating surface water vapor content via radar refractivity is part of the planned next-generation radar (NEXRAD) enhancements (Saffle et al. 2006), therefore it is desirable to validate the potential usefulness of the refractivity-based vapor mixing ratio derivation technique for forecasters.

Following Fabry et al. (1997), Fabry (2004), and Bean and Dutton (1968), the water vapor mixing ratio can be calculated from a combination of radar refractivity with surface temperature and pressure measurements. Combining interpolated S-Pol refractivity fields obtained using the radar objective analysis described in

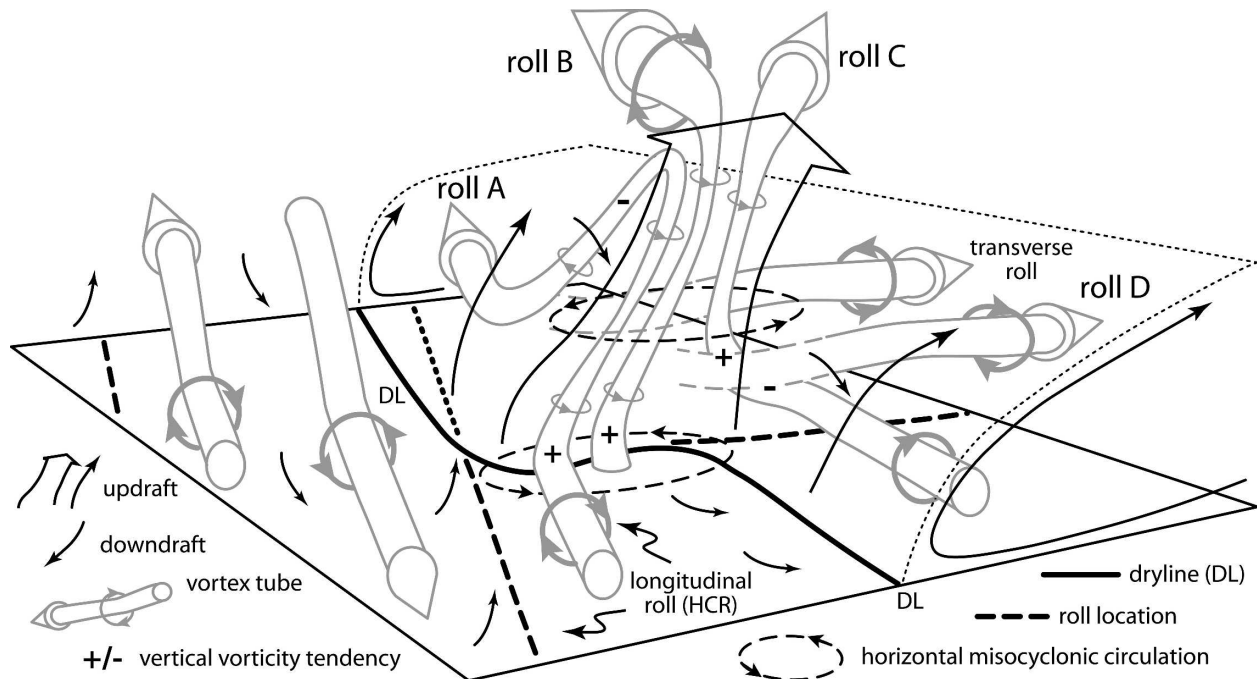


FIG. 22. Conceptual model of misocyclones embedded within the dryline on 22 May 2002. Vortex tubes associated with HCRs, transverse rolls, the dryline, and the misocyclone are shown in gray. The heavy solid line denotes the dryline location and the thin dotted black line indicates the moist layer.

section 2b together with the Lagrangian surface temperature field and a mean mobile mesonet pressure value obtained at matching analysis times, the fields of refractivity-based water vapor mixing ratio have been derived.

There is a reasonable correspondence between the locations and magnitudes of the moisture gradient at the dryline between the refractivity-based and Lagrangian analyses (Fig. 23 versus Fig. 10, respectively). In particular, the refractivity-based and Lagrangian analyses reveal comparable trends of drying to the west of the dryline with an increasing across-dryline moisture gradient and mean westward dryline movement. These results are consistent with Weckwerth et al. (2005), who compared the S-Pol refractivity with the refractivity computed from individual surface station, aircraft, and mobile mesonet observations on this day. Notable differences between the results of the contrasting analysis methods include the small-scale features east of the dryline seen in the refractivity-based analyses, with the very dry areas that coincide with S-Pol radials (e.g., Fig. 23d) possibly caused by beam blockage (e.g., Weckwerth et al. 2005) and the very dry or exceptionally moist pockets east of the dryline possibly related to unrealistically low or high values of refractivity caused by moving ground targets or vegetation sway (Fabry 2004; Weckwerth et al. 2005).

Except for localized areas that may be contaminated by beam blockage or other refractivity errors in combination with the effects of Lagrangian analysis assumptions, the differences between the two moisture field analysis methods are rather small (Fig. 24). In particular, after removing areas with possible beam blockage effects the average difference between the entire time series of refractivity-based and Lagrangian analyses is only about 0.5 g kg^{-1} or less. A good correspondence between the two independent moisture analyses validates each approach and further demonstrates the potential utility of the refractivity-based and Lagrangian moisture analysis techniques.

f. Relationship between BL moisture and differential reflectivity

The present study has demonstrated that the water vapor mixing ratio field in the BL may be obtained by exploiting a simple continuity relationship in which air parcels follow the radar-derived airflow as passive tracer variables. In particular, it has been shown that undulations or plumes of vapor mixing ratio in the BL correspond to positions of updrafts and collocated reflectivity plumes, implying that the radar scatterer and passive tracer fields may exhibit a similar continuity relationship with respect to the BL airflow. Differential reflectivity (Z_{DR}), the ratio of the returned powers of

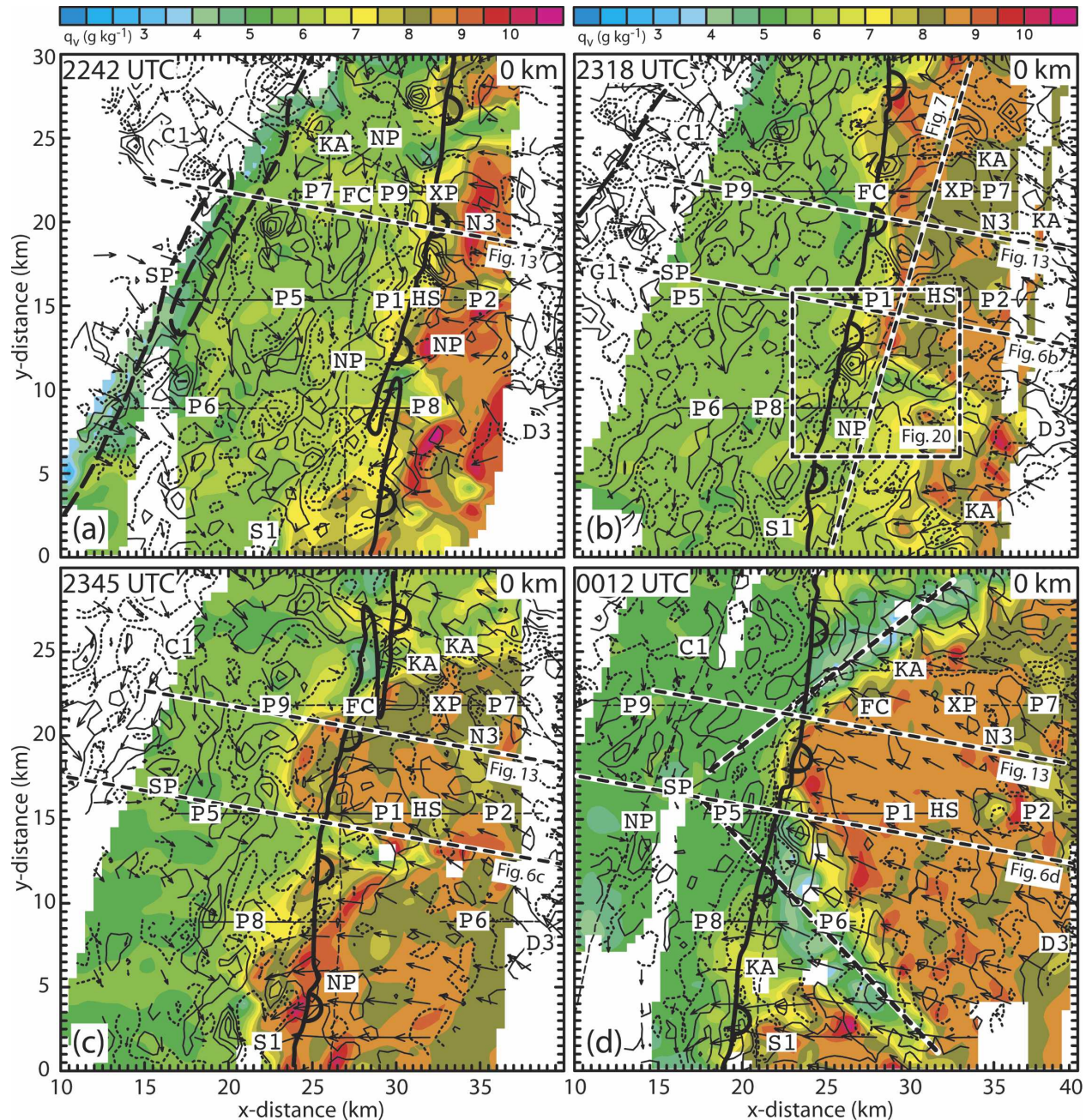


FIG. 23. Water vapor mixing ratio (g kg^{-1}) analyses near the surface derived from the S-Pol refractivity data and the thermodynamic analyses as described in the text. Also plotted are horizontal wind vectors ($1 \text{ km} = 4 \text{ m s}^{-1}$) and vertical vorticity (s^{-1}) every $2 \times 10^{-3} \text{ s}^{-1}$ with positive values (black solid lines) starting at $1 \times 10^{-3} \text{ s}^{-1}$ and negative values (black dotted line) starting at $-1 \times 10^{-3} \text{ s}^{-1}$. The thick black dashed lines indicate areas of beam blockage. The dryline locations are also shown. Compare with the water vapor mixing ratio analyses obtained through the synthesis of in situ data (Fig. 10).

the horizontal and vertical components of a polarimetric radar beam, has demonstrated utility in differentiating various types of scatterers at S-band wavelengths. For example, Wilson et al. (1994) and Zrníc and Ryzhkov (1998) employed 11-cm polarimetric radar measurements and theoretical scattering models to show

that the origin of clear-air echoes in the warm-season BL are insects. Wilson et al. (1994) demonstrated that reflectivity plumes and thin lines are caused by a concentration of insects at altitude in BL updrafts, a finding that is strongly supported by the present radar analysis results (e.g., Figs. 6, 7, 21). In consideration of the pend-

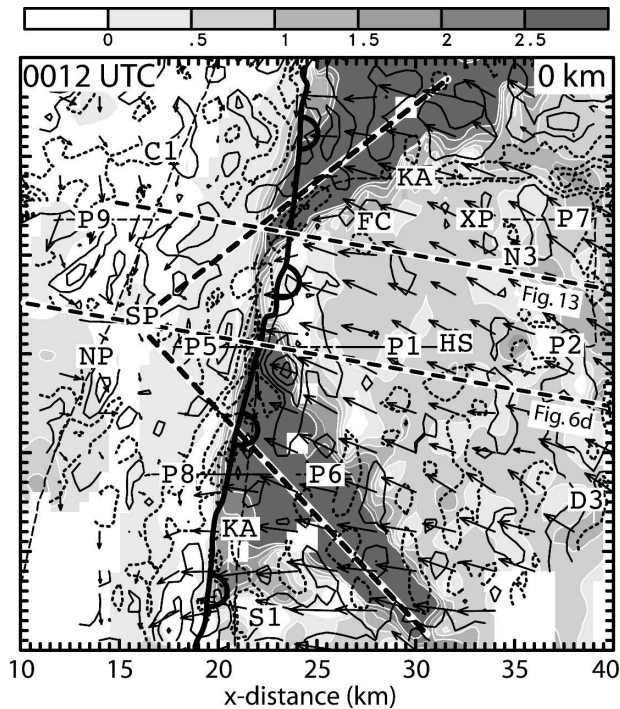


FIG. 24. As in Fig. 23, but showing the difference field at 0012 UTC between the water vapor mixing ratio analyses obtained through the synthesis of the in situ data (Fig. 10d) and derived from the S-Pol refractivity data (Fig. 23d).

ing upgrade of the Weather Surveillance Radar-1998 Doppler radar network to polarization diversity during the next 5–10 yr (Crum et al. 1998; Saffle et al. 2006), the following analysis and discussion explores the hypothesis that operational Z_{DR} measurements may provide useful information regarding the character of the BL water vapor mixing ratio fields owing to airflow continuity constraints.

Geerts and Miao (2005a) have shown that insects may exhibit an active though limited response to vertical BL motion (i.e., the updraft opposition scenario of Geerts and Miao 2005b), either increasing or decreasing their downward motion with respect to still air in the presence of updraft or downdraft, respectively. Geerts and Miao (2005b) used a simple 2D kinematic model of insect concentration in parameterized BL rolls to show that insect concentrations attained an absolute maximum value in the midlevel updraft core of a roll in the “updraft opposition” scenario, whereas the case where insects had no fall speed produced a deeper concentration core in the updraft region extending from the surface toward the top of the roll. In effect, insects with larger downward motion in stronger updrafts tend to concentrate in the updraft core in agreement with the hypothesis of Wilson et al. (1994). Thus,

the zero-fall speed case of Geerts and Miao (2005b) is conceptually analogous to the water vapor mixing ratio plume forced by the secondary dryline circulation in the present case (Figs. 13, 21). Assuming there is some distribution of insect size and that large insects fall faster than small insects, size sorting would be expected to occur with larger insects collecting in midlevels and smaller insects being carried to the top of the updraft (Wilson et al. 1994). Owing to Z_{DR} increasing with insect size or effective cross section (Wilson et al. 1994; Zrnic and Ryzhkov 1998) as well as to the aforementioned size sorting and updraft opposition effects, it is hypothesized that Z_{DR} may develop a midlevel relative maximum in strong updrafts. Conversely, it is hypothesized that a layer of high Z_{DR} may develop in weaker, shallower convective BL updrafts due to confinement of the insects close to ground (e.g., Johnson 1957; Isard et al. 1990).

Objectively analyzing Z_{DR} data from S-Pol data on 22 May following methods described in section 2b, plumes of high Z_{DR} are concentrated within the moist dryline updraft and secondary circulation in broad consistency with the previously mentioned size sorting and updraft opposition controls on insect size and concentration (Fig. 25). Analyzed high Z_{DR} plumes are collocated with reflectivity plumes (Fig. 25 versus Fig. 6), although it appears possible to discriminate between comparable reflectivities on either side of the dryline using high Z_{DR} . A shallow Z_{DR} layer containing relatively weak Z_{DR} cores and plumes is confined within the moist BL east of the dryline (Fig. 25), consistent with the notion that insects are confined and concentrated in the moist BL in the absence of deep, penetrative updrafts that would vent insects into the overlying ERL. Several strongly eastward-sloping Z_{DR} plumes are also noted within the ERL to the east of the dryline, suggesting that detrainment from updraft plumes and subsequent horizontal transport of insects may produce elevated insect-containing layers (e.g., Isard et al. 1990) corresponding to the elevated Z_{DR} layers. Finally, maximum Z_{DR} values west of the dryline are significantly smaller than in the moist BL east of the dryline, presumably due to deep vertical mixing which in turn would be expected to lower the overall insect concentrations. The joint values of Z_{DR} (i.e., approximately 2–10 dB) and reflectivity (i.e., approximately 10–20 dBZ) at common locations (e.g., Fig. 25 versus Fig. 6) are consistent with the observations and theoretical predictions of the Wilson et al. (1994) and Zrnic and Ryzhkov (1998) studies of S-band insect scattering in the BL. The combined airflow, water vapor mixing ratio, and Z_{DR} analyses support the hypothesis that similar continuity relationships exist between airflow and

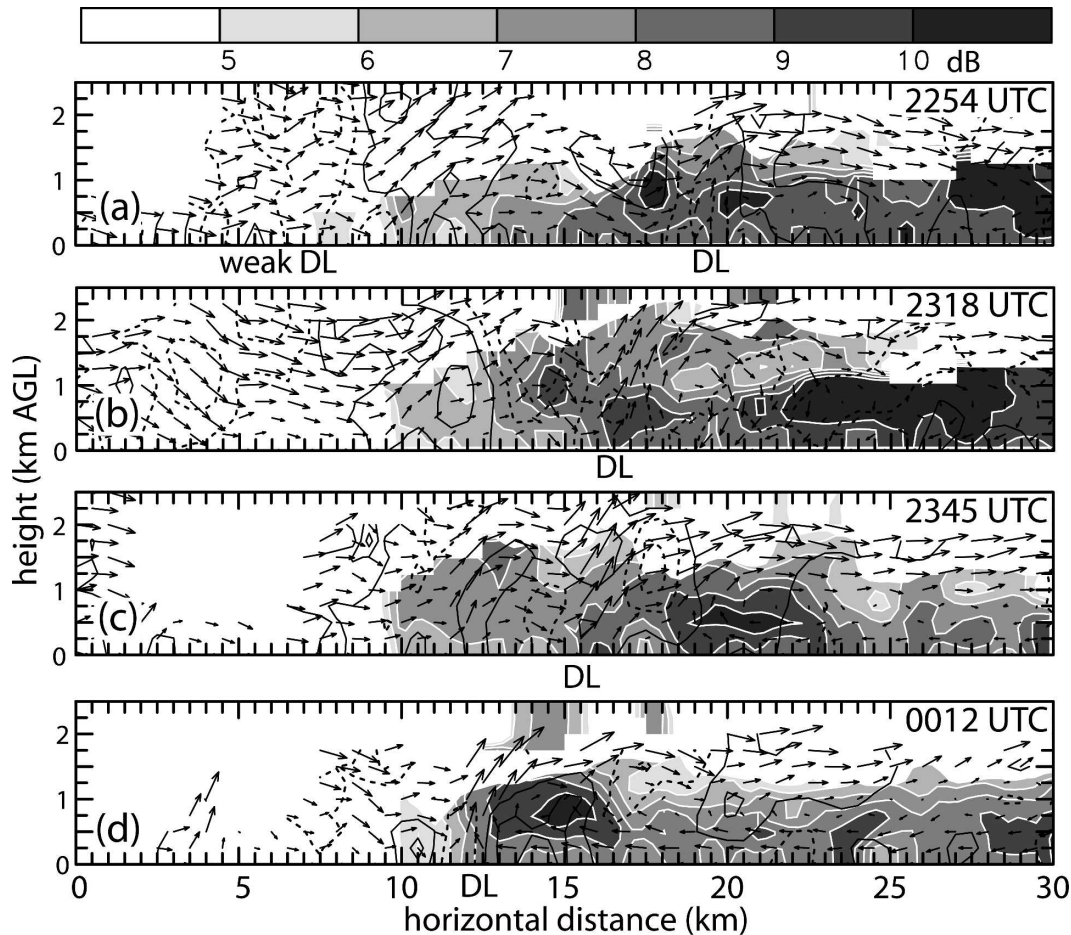


FIG. 25. Differential reflectivity [Z_{DR} (dB)] obtained from S-Pol on 22 May 2002. The locations of the cross sections are shown in Fig. 4. Contours and vectors are as in Fig. 6.

either water vapor mixing ratio or insect size and concentration, with updraft opposition by insects possibly contributing to Z_{DR} maxima in updraft cores.

5. Conclusions

This paper presents Lagrangian analysis of the 3D structure and evolution of the dryline and the surrounding BL on 22 May 2002 using mobile ground-based radar and in situ data obtained during the IHOP field experiment. Using the time-varying 3D wind fields, trajectories are computed from the in situ mesonet, aircraft, and gridpoint pseudosounding data locations. The observed θ_w , θ , and q_w data are then advected along trajectories and objectively analyzed to the grid using a two-pass Barnes scheme that includes both space and time weighting. A high-resolution Lagrangian analysis in a misocyclone-relative reference frame with reduced Lagrangian smoothing elucidates details of the moisture structure of a misocyclone embedded in the

dryline. Inferences of the processes of dryline formation and movement, misocyclone effects on dryline moisture gradients, and cloud development are facilitated by these kinematic and Lagrangian BL analyses.

The 22 May 2002 dryline is characterized by a nearly north-south-oriented band of enhanced reflectivity and vertical velocity residing in a zone of confluence and a pronounced secondary circulation that is able to lift dry air to the west over the surface dryline location. A second, minor dryline is located west of the primary dryline. Initially, the dryline is nearly stationary and convection in the CBL west of the dryline exhibits a complex structure of open cellular and banded features. As HCRs eventually become the dominant convective mode west of the dryline, transverse rolls develop in the moist layer. Concurrent with roll development, strong vortices and associated dryline waves develop near the intersections of the dryline with rolls. As surface heating decreases, the BL convection west of the dryline becomes weaker and more disorganized, the smaller

scale vortices are replaced with larger scale (~ 15 km) waves, and the dryline retrogrades to the west.

Mobile mesonet data reveal across-dryline gradients of q_v and θ_v typically of order $2\text{--}4 \text{ g kg}^{-1} \text{ km}^{-1}$ and 0.25 K km^{-1} , respectively. Three distinct profile types are manifested in the individual mobile mesonet dryline traverses. The moisture profiles are characterized by nearly constant values on either of the dryline with single or multiple sharp steplike across-dryline moisture changes, although localized moisture minima are also observed which suggest an inflected or S-shaped dryline orientation not previously reported. The variations in the moisture profiles are most likely caused by varying degrees of mixing between the dry and moist BLs, in turn controlled by the strength of the secondary circulation and locally modulated by misovortices embedded within the dryline.

The Lagrangian thermodynamic analysis reveals that the q_v and θ_v gradients reside within or very near the confluence zone noted in the wind fields. The vertical structure of the dryline is characterized by a warm, moist internal BL capped by the deeper hot, dry BL that advects over the surface dryline from the west. In the lower levels, convergence on the dryline is frontogenetic and acts to generate the q_v and θ_v gradients, whereas the airflow in the upper levels of the BL is divergent and frontolytic, thereby tilting the horizontal gradients into the vertical. The secondary circulation along the dryline is primarily forced by the buoyancy solenoid term in the vorticity equation, and this circulation acts to enhance the dryline updraft and generate westerly shear through the moist BL and the ERL.

There is generally a good correspondence in the magnitude and the location of the dryline gradient between the Lagrangian and refractivity-based q_v analyses and reflectivity thin-line echoes. The magnitudes and time trends of the moisture values on the dry and moist sides of the dryline and the dryline location are similar in the two analyses. It has been shown that Z_{DR} can be used to differentiate the BL structure on either side of the dryline. The highest Z_{DR} values (5–10 dB), associated with small insect scatterers, are concentrated within the moist air east of the dryline. Therefore, there is potential to infer the dryline location and BL character by combining reflectivity, refractivity, and Z_{DR} measurements along with Doppler velocity convergence at low elevation angles.

Persistent airflow features are reported in this study, including updrafts, small-scale vortices (i.e., misocyclones), and a dryline-normal secondary circulation, whose temporal coherence implies a level of BL predictability. Of particular interest are the BL vortices, several of which propagate from south to north along

the dryline and are tracked across the analysis domain (30 km) for up to 30 min or longer. As a particularly intense vortex moves along the dryline, its horizontal circulation produces an undulation or wave on the dryline with deep moisture to its north and shallow moisture to its south. Hypothetically, a procession of such dryline vortices may thus act to episodically force the dryline eastward via successive vortex passages.

Acknowledgments. The authors gratefully acknowledge contributions by Alan Shapiro and Howard Bluestein (OU), who reviewed an earlier version of this manuscript, by Robert Rabin (NSSL) who re navigated and gridded GOES-8 satellite imagery, and by David Stensrud (NSSL) who analyzed the inflection point instability with the Stensrud–Shirer model. Peggy Lemone and an anonymous reviewer provided comments that improved the manuscript. Partial funding for this research was provided by National Science Foundation (NSF) Grant ATM-0130316. Funding for DOW radar deployment and post-analysis was provided under NSF Grant ATM-0208651.

REFERENCES

- André, J. C., G. De Moor, P. Lacarrère, and R. du Vachat, 1978: Modeling the 24-hour evolution of the mean and turbulent structures of the planetary boundary layer. *J. Atmos. Sci.*, **35**, 1861–1883.
- Anthes, R. A., Y. Kuo, S. G. Benjamin, and Y. Li, 1982: The evolution of the mesoscale environment of severe local storms: preliminary modeling results. *Mon. Wea. Rev.*, **110**, 1187–1213.
- Arnott, N. R., Y. P. Richardson, J. M. Wurman, and J. Lutz, 2003: A solar alignment technique for determining mobile radar pointing angles. Preprints, *31st Int. Conf. on Radar Meteorology*, Seattle, WA, Amer. Meteor. Soc., 492–494.
- Atkins, N. T., R. M. Wakimoto, and C. L. Ziegler, 1998: Observations of the finescale structure of the dryline during VORTEX 95. *Mon. Wea. Rev.*, **126**, 525–549.
- Barnes, S. L., 1973: Mesoscale objective analysis using weighted time-series observations. NOAA Tech. Memo. ERL NSSL-62, National Severe Storms Laboratory, 60 pp.
- Bean, B. R., and E. J. Dutton, 1968: *Radio Meteorology. National Bureau of Standards Monogr.*, No. 92, National Bureau of Standards, 435 pp.
- Betts, A. K., 1984: Boundary layer thermodynamics of a High Plains severe storm. *Mon. Wea. Rev.*, **112**, 2199–2211.
- Biggerstaff, M., and Coauthors, 2005: The Shared Mobile Atmospheric Research and Teaching (SMART) radar: A collaboration to enhance research and teaching. *Bull. Amer. Meteor. Soc.*, **86**, 1263–1274.
- Bluestein, H. B., 1993: *Synoptic-Dynamic Meteorology in Midlatitudes*. Vol. 2. *Observations and Theory of Weather Systems*, Oxford University Press, 594 pp.
- , and S. S. Parker, 1993: Modes of isolated, severe convective storm formation along the dryline. *Mon. Wea. Rev.*, **121**, 1354–1372.
- , E. W. McCaul Jr., G. P. Byrd, and G. R. Woodall, 1988:

- Mobile sounding observations of a tornadic storm near the dryline: The Canadian, Texas Storm of 7 May 1986. *Mon. Wea. Rev.*, **116**, 1790–1804.
- Brown, R. A., 1980: Longitudinal instabilities and secondary flows in the planetary boundary layer: A review. *Rev. Geophys. Space Phys.*, **18**, 683–697.
- Brümmer, B., 1985: Structure, dynamics, and energetics of boundary layer rolls from KonTur aircraft observations. *Contrib. Atmos. Phys.*, **58**, 237–254.
- Buban, M., 2005: The dryline on 22 May 2002 during IHOP: Ground-radar and in situ data analyses of the dryline and boundary layer evolution. M.S. thesis, University of Oklahoma, Norman, 73 pp. [Available from UMI, 300 North Zeeb Road, P.O. Box 1346, Ann Arbor, MI 48106-1346.]
- Carbone, R. E., 1982: A severe frontal rainband. Part I: Storm-wide hydrodynamic structure. *J. Atmos. Sci.*, **39**, 258–279.
- Crawford, T. M., and H. B. Bluestein, 1997: Characteristics of dryline passage during COPS-91. *Mon. Wea. Rev.*, **125**, 463–477.
- Crum, T. D., R. E. Saffle, and J. W. Wilson, 1998: An update on the NEXRAD program and future WSR-88D support to operations. *Wea. Forecasting*, **13**, 253–262.
- Demoz, B., and Coauthors, 2006: The dryline on 22 May 2002 during IHOP 2002: Convective-scale measurements at the profiling site. *Mon. Wea. Rev.*, **134**, 294–310.
- Doswell, C. A., III, 1985: Reply. *J. Atmos. Sci.*, **42**, 2076–2079.
- Fabry, F., 2004: Meteorological value of ground target measurements by radar. *J. Atmos. Oceanic Technol.*, **21**, 560–573.
- , C. Frush, I. Zawadzki, and A. Kilambi, 1997: On the extraction of near-surface index of refraction using radar phase measurements from ground targets. *J. Atmos. Oceanic Technol.*, **14**, 978–987.
- Geerts, B., and Q. Miao, 2005a: The use of millimeter Doppler radar echoes to estimate vertical air velocities in the fair-weather convective boundary layer. *J. Atmos. Oceanic Technol.*, **22**, 225–246.
- , and —, 2005b: A simple numerical model of the flight behavior of small insects in the atmospheric convective boundary layer. *Environ. Entomol.*, **34**, 353–360.
- Gossard, E., and W. Moninger, 1975: The influence of a capping inversion on the dynamic and convective instability of a boundary layer model with shear. *J. Atmos. Sci.*, **32**, 2111–2124.
- Hane, C. E., C. L. Ziegler, and H. B. Bluestein, 1993: Investigation of the dryline and convective storms initiated along the dryline: Field experiments during COPS-91. *Bull. Amer. Meteor. Soc.*, **74**, 2133–2145.
- , H. B. Bluestein, T. M. Crawford, M. E. Baldwin, and R. M. Rabin, 1997: Severe thunderstorm development in relation to along-dryline variability: A case study. *Mon. Wea. Rev.*, **125**, 231–251.
- , M. E. Baldwin, H. B. Bluestein, T. M. Crawford, and R. M. Rabin, 2001: A case study of severe storm development along a dryline within a synoptically active environment. Part I: Dryline motion and an Eta model forecast. *Mon. Wea. Rev.*, **129**, 2183–2204.
- Houze, R. A., Jr., 1993: *Cloud Dynamics*. Academic Press, 573 pp.
- Isard, S. A., M. E. Irwin, and S. E. Hollinger, 1990: Vertical distribution of aphids (Homoptera: Aphididae) in the planetary boundary layer. *Environ. Entomol.*, **19**, 1473–1484.
- Johns, R. H., and C. A. Doswell III, 1992: Severe local storms forecasting. *Wea. Forecasting*, **7**, 588–612.
- Johnson, C. G., 1957: The vertical distribution of aphids in the air and the temperature lapse rate. *Quart. J. Roy. Meteor. Soc.*, **83**, 194–201.
- Kanak, K. M., D. K. Lilly, and J. T. Snow, 2000: The formation of vertical vortices in the convective boundary layer. *Quart. J. Roy. Meteor. Soc.*, **126**, 2789–2810.
- Karan, H., and K. Knupp, 2006: Mobile Integrated Profiler System (MIPS) observations of low-level convergent boundaries during IHOP. *Mon. Wea. Rev.*, **134**, 92–112.
- Kingsmill, D. E., 1995: Convection initiation associated with a sea-breeze front, a gust front, and their collision. *Mon. Wea. Rev.*, **123**, 2913–2933.
- Koch, S. E., and J. McCarthy, 1982: The evolution of an Oklahoma dryline. Part II: Boundary-layer forcing of mesoconvective systems. *J. Atmos. Sci.*, **39**, 237–257.
- , M. DesJardins, and P. Kocin, 1983: An interactive Barnes objective map analysis scheme for use with satellite and conventional data. *J. Climate Appl. Meteor.*, **22**, 1487–1503.
- , 1979: Mesoscale gravity waves as a possible trigger for severe convection along a dryline. Ph.D. dissertation, University of Oklahoma, 195 pp. [Available from UMI, 300 North Zeeb Road, P.O. Box 1346, Ann Arbor, MI 48106-1346.]
- Kundu, P. K., 2002: *Fluid Mechanics*. Academic Press, 730 pp.
- Laird, N. F., D. A. R. Kristovich, R. M. Rauber, H. T. Ochs III, and L. J. Miller, 1995: The Cape Canaveral sea and river breezes: Kinematic structure and convective initiation. *Mon. Wea. Rev.*, **123**, 2942–2956.
- Lilly, D. K., 1966: On the instability of Ekman boundary flow. *J. Atmos. Sci.*, **23**, 481–494.
- Mahoney, W. P., III, 1988: Gust front characteristics and the kinematics associated with interacting thunderstorm outflows. *Mon. Wea. Rev.*, **116**, 1474–1492.
- Marquis, J., Y. P. Richardson, and J. M. Wurman, 2007: Kinematic observations of mesocyclones along boundaries during IHOP. *Mon. Wea. Rev.*, **135**, 1749–1768.
- McCarthy, J., and S. E. Koch, 1982: The evolution of an Oklahoma dryline. Part I: A meso- and subsynoptic-scale analysis. *J. Atmos. Sci.*, **39**, 225–236.
- McNulty, R. P., 1995: Severe and convective weather: A central region forecasting challenge. *Wea. Forecasting*, **10**, 187–202.
- Mohr, C. G., L. J. Miller, R. L. Vaughan, and H. W. Frank, 1986: The merger of mesoscale datasets into a common Cartesian format for efficient and systematic analyses. *J. Atmos. Oceanic Technol.*, **3**, 144–161.
- Nielsen, J. W., and P. P. Neille, 1990: The vertical structure of New England coastal fronts. *Mon. Wea. Rev.*, **118**, 1793–1807.
- Ogura, Y., and Y. Chen, 1977: A life history of an intense mesoscale convective storm in Oklahoma. *J. Atmos. Sci.*, **34**, 1458–1476.
- , H. Juang, K. Zhang, and S. Soong, 1982: Possible triggering mechanisms for severe storms in SESAME-AVE IV (9–10 May 1979). *Bull. Amer. Meteor. Soc.*, **63**, 503–515.
- Oye, R., C. Mueller, and S. Smith, 1995: Software for radar translation, visualization, editing, and interpolation. Preprints, 27th Conf. on Radar Meteorology, Vail, CO, Amer. Meteor. Soc., 359–361.
- Parsons, D. B., M. A. Shapiro, R. M. Hardesty, R. J. Zamora, and J. M. Intrieri, 1991: The finescale structure of a west Texas dryline. *Mon. Wea. Rev.*, **119**, 1242–1258.
- Pielke, R. A., Sr., 1984: *Mesoscale Meteorological Modeling*. Academic Press, 612 pp.
- Pietrycha, A. E., and E. N. Rasmussen, 2004: Finescale surface

- observations of the dryline: A mobile mesonet perspective. *Wea. Forecasting*, **19**, 1075–1088.
- Rasmussen, N. E., R. Davies-Jones, C. A. Doswell Jr., F. H. Carr, M. D. Eilts, D. R. MacGorman, J. M. Straka, and F. H. Carr, 1994: Verification of the Origins of Rotation in Tornadoes Experiment: VORTEX. *Bull. Amer. Meteor. Soc.*, **75**, 995–1006.
- Rhea, J. O., 1966: A study of thunderstorm formation along drylines. *J. Appl. Meteor.*, **5**, 58–63.
- Rust, W. D., R. P. Davies-Jones, D. W. Burgess, R. A. Maddox, L. C. Showell, T. C. Marshall, and D. K. Lauritsen, 1990: Testing a mobile version of a cross-chain Loran atmospheric sounding system (M-CLASS). *Bull. Amer. Meteor. Soc.*, **71**, 173–180.
- Saffle, R. E., M. J. Istok, and G. Cate, 2006: NEXRAD product improvement—Expanding science horizons. Preprints, *22d Conf. on Interactive Information Processing Systems*, Atlanta, GA, Amer. Meteor. Soc., CD-ROM, 9.1.
- Schaefer, J. T., 1974: A simulative model of dryline motion. *J. Atmos. Sci.*, **31**, 956–964.
- Shirer, H. N., 1986: On cloud street development in three dimensions: Parallel and Rayleigh instabilities. *Contrib. Atmos. Phys.*, **59**, 126–149.
- Stensrud, D. J., and H. N. Shirer, 1988: Development of boundary layer rolls from dynamic instabilities. *J. Atmos. Sci.*, **45**, 1007–1019.
- Straka, J. M., E. N. Rasmussen, and S. E. Fredrickson, 1996: A mobile mesonet for finescale meteorological observations. *J. Atmos. Oceanic Technol.*, **13**, 921–936.
- Sun, W.-Y., 1987: Mesoscale convection along the dryline. *J. Atmos. Sci.*, **44**, 1394–1403.
- , and Y. Ogura, 1979: Boundary layer forcing as a possible trigger to a squall-line formation. *J. Atmos. Sci.*, **36**, 235–254.
- , and C. Wu, 1992: Formation and diurnal variation of the dryline. *J. Atmos. Sci.*, **49**, 1606–1619.
- Wakimoto, R. M., 1982: The life cycle of thunderstorm gust fronts as viewed with Doppler radar and rawinsonde data. *Mon. Wea. Rev.*, **110**, 1060–1082.
- , C. Liu, and H. Cai, 1998: The Garden City, Kansas, storm during VORTEX 95. Part I: Observations of the storm's life-cycle and tornadogenesis. *Mon. Wea. Rev.*, **126**, 372–392.
- Weckwerth, T. M., and D. B. Parsons, 2006: A review of convection initiation and motivation for IHOP_2002. *Mon. Wea. Rev.*, **134**, 5–22.
- , J. W. Wilson, R. M. Wakimoto, and N. A. Crook, 1997: Horizontal convective rolls: Determining the environmental conditions supporting their existence and characteristics. *Mon. Wea. Rev.*, **125**, 505–526.
- , and Coauthors, 2004: An overview of the International H₂O Project (IHOP_2002) and some preliminary highlights. *Bull. Amer. Meteor. Soc.*, **85**, 253–277.
- , C. R. Pettet, F. Fabry, S. Park, M. A. LeMone, and J. W. Wilson, 2005: Radar refractivity retrieval: Validation and application to short-term forecasting. *J. Appl. Meteor.*, **44**, 285–300.
- Weiss, C. C., and H. B. Bluestein, 2002: Airborne pseudo-dual Doppler analysis of a dryline–outflow boundary intersection. *Mon. Wea. Rev.*, **130**, 1207–1226.
- , —, and A. L. Pazmany, 2006: Finescale radar observations of the 22 May 2002 dryline during the International H₂O Project (IHOP). *Mon. Wea. Rev.*, **134**, 273–293.
- Wilson, J. W., T. M. Weckwerth, J. Vivekanandan, R. M. Wakimoto, and R. W. Russell, 1994: Boundary layer clear-air echoes: Origin of echoes and accuracy of derived winds. *J. Atmos. Oceanic Technol.*, **11**, 1184–1206.
- Wurman, J., J. Straka, E. Rasmussen, M. Randall, and A. Zahrai, 1997: Design and deployment of a portable, pencil-beam, pulsed, 3-cm Doppler radar. *J. Atmos. Oceanic Technol.*, **14**, 1502–1512.
- , 2001: The DOW mobile multiple Doppler network. Preprints, *30th Int. Conf. on Radar Meteorology*, Munich, Germany, Amer. Meteor. Soc., 95–97.
- Ziegler, C. L., and C. E. Hane, 1993: An observational study of the dryline. *Mon. Wea. Rev.*, **121**, 1489–1506.
- , and E. N. Rasmussen, 1998: The initiation of moist convection at the dryline: Forecasting issues from a case study perspective. *Wea. Forecasting*, **13**, 1106–1131.
- , W. J. Martin, R. A. Pielke, and R. L. Walko, 1995: A modeling study of the dryline. *J. Atmos. Sci.*, **52**, 263–285.
- , T. J. Lee, and R. A. Pielke Sr., 1997: Convective initiation at the dryline: A modeling study. *Mon. Wea. Rev.*, **125**, 1001–1026.
- , E. N. Rasmussen, T. R. Shepherd, A. I. Watson, and J. M. Straka, 2001: The evolution of low-level rotation in the 29 May 1994 Newcastle-Graham, Texas, storm complex during VORTEX. *Mon. Wea. Rev.*, **129**, 1339–1368.
- , D. Kennedy, and E. N. Rasmussen, 2004: A wireless network for collection and synthesis of mobile mesoscale weather observations. *J. Atmos. Oceanic Technol.*, **21**, 1659–1669.
- , M. S. Buban, and E. N. Rasmussen, 2007: A Lagrangian objective analysis technique for assimilating in situ observations with multiple radar-derived airflow. *Mon. Wea. Rev.*, **135**, 2417–2442.
- Znic, D. S., and A. V. Ryzhkov, 1998: Observations of insects and birds with a polarimetric radar. *IEEE Trans. Geosci. Remote Sens.*, **36**, 661–668.